



# Particle focusing in a wavy channel

Xinyu Mao<sup>1</sup>, Irmgard Bischofberger<sup>1</sup> and A.E. Hosoi<sup>1,2,†</sup>

<sup>1</sup>Department of Mechanical Engineering, Massachusetts Institute of Technology, Cambridge, MA 02139, USA

<sup>2</sup>Department of Mathematics, Massachusetts Institute of Technology, Cambridge, MA 02139, USA

(Received 18 February 2023; revised 14 June 2023; accepted 5 July 2023)

---

It is known that inertial lift forces can lead to particle focusing in channel flows; yet oscillatory straining effects have also been suggested as a mechanism for particle focusing in wavy channels. To explore the synergy between these two mechanisms, we analytically and experimentally investigate the focusing behaviour of rigid neutrally buoyant particles in a wavy channel. We decompose the particle-free channel flow into a primary Poiseuille flow and secondary eddies induced by the waviness. We calculate the perturbation of the particle on the particle-free flow and the resulting lateral lift force exerted on the particle using the method of matched asymptotic expansions. This yields a zeroth-order lift force arising from the Poiseuille flow and a first-order lift force due to the waviness of the channel. We further incorporate the inertial lift force into the Maxey–Riley equation and simulate particle trajectories in wavy channels. The interactions between the zeroth-order lift force and the particle-free flow largely determine the focusing locations. Experiments in wavy channels with varying amplitudes at channel Reynolds numbers ranging from 5 to 250 are consistent with the predictions of the focusing locations, which are mainly governed by the channel Reynolds number as well as the competition between the inertial lift and the oscillatory straining effects.

**Key words:** particle/fluid flow, microfluidics, suspensions

---

## 1. Introduction

Randomly distributed particles can spontaneously migrate across streamlines in channel flows and eventually focus at specific regions or locations within the cross-section. In the pioneering experimental work of Segré & Silberberg (1961), particles migrate across streamlines and focus into a ring in a circular pipe. Since then, experimental studies have extensively investigated particle focusing in straight channels by varying the channel Reynolds number, the shape of the channel cross-section and the particle size (Matas, Morris & Guazzelli 2004; Di Carlo *et al.* 2009; Morita, Itano & Sugihara-Seki 2017;

† Email address for correspondence: [peko@mit.edu](mailto:peko@mit.edu)

Nakayama *et al.* 2019). The inertial lift force has long been identified as the mechanism driving lateral migration of particles and thus as the key to understanding the physics underlying particle focusing (Saffman 1965). Previous theoretical work has employed asymptotic analysis (Cox & Brenner 1968; Ho & Leal 1974; Schonberg & Hinch 1989; Hogg 1994; Asmolov 1999; Matas, Morris & Guazzelli 2009; Hood, Lee & Roper 2015), numerical simulations (Asmolov *et al.* 2018; Bazaz *et al.* 2020) and, more recently, machine learning (Su *et al.* 2021) to calculate the variation of the lift force on a particle in a straight channel. These studies provided reliable predictions for the focusing conditions and the equilibrium locations of particles.

Driven by microfluidic applications, the past twenty years have witnessed a variety of particle focusing techniques featuring non-standard channel structures. These structures include spiral channels (Bhagat, Kuntaegowdanahalli & Papautsky 2008; Harding, Stokes & Bertozzi 2019), asymmetric or symmetric serpentine channels (Di Carlo *et al.* 2007, 2008), expansion–contraction channels (Park, Song & Jung 2009; Zhou, Kasper & Papautsky 2013), pillar arrays in straight channels (Amini *et al.* 2013), grooved or textured channels (Nizkaya *et al.* 2020; Zhang *et al.* 2021), channels with unconventional cross-sections (Kim *et al.* 2016) and permeate channels (Garcia & Pennathur 2017; Garcia, Ganapathysubramanian & Pennathur 2019). Many non-standard channels demonstrate the potential to reduce the footprint of the device and to improve focusing performance relative to straight channels, as characterized by the reduction in the required channel length and pressure for the focusing of sub-micron particles (Tang *et al.* 2020). On top of the zeroth-order Poiseuille flow, non-standard channels introduce secondary flows that are the reason for the improved performance (Tang *et al.* 2020). Most studies still acknowledge the role of the inertial lift force in particle focusing (Zhang *et al.* 2016). However, due to the existence of secondary flows, the variations of the inertial lift force are poorly understood in many non-standard channels (Stoecklein & Di Carlo 2019). Quantitative predictions of the focusing locations in curved ducts have been explored based on the balance between the inertial lift force and other hydrodynamic forces arising from the secondary flows (Harding *et al.* 2019; Harding & Stokes 2020; Ha *et al.* 2022; Valani, Harding & Stokes 2022). However, the focusing locations remain to be explored in many other types of non-standard channels.

One common feature of many non-standard channels is periodicity along the axial direction (figure 1). For example, the centreline of a serpentine channel can be described by a sinusoidal function. The curvature introduces a secondary Dean flow that is perpendicular to the axial direction (Di Carlo *et al.* 2007). The Dean flow emerges due to the mismatch in the velocity across the channel cross-section and the resultant centrifugal pressure gradient. The balance between the inertial lift force and the drag force associated with the Dean flow determines the equilibrium positions of the particles (Di Carlo *et al.* 2007). As a second example, the centreline of an expansion–contraction channel follows a straight line, but its walls have a periodic square waveform. Thus, vortices form at the abrupt expansions. Depending on the interplay between the inertial lift force and the vortices, particles can either be trapped in the expanded regions or migrate towards the inner part of the channel (Park *et al.* 2009; Zhou *et al.* 2013). In these two examples, the periodic channels significantly differ from straight channels in that the secondary flows are of equal importance to the inertial lift force in determining the particles' behaviour. Similarly, when periodic channels only moderately deviate from straight channels, a less noticeable secondary flow may give rise to different focusing mechanisms. Hewitt & Marshall (2010) investigated particle focusing in a corrugated tube with a radius varying sinusoidally along the axial direction. By neglecting the lift force on the particles and employing lubrication theory for the channel flow, they analytically

## Particle focusing in a wavy channel

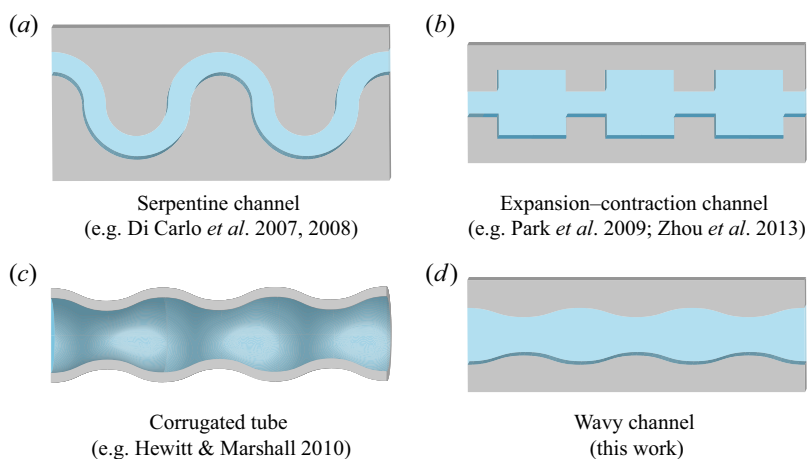


Figure 1. Schematics of several types of periodic channels discussed in the literature.

found that particles focus on the centreline of the tube. This behaviour was also revealed in their discrete-element simulations in which a Saffman lift force acts on the particles. They attributed particle focusing to the alternating series of positive and negative strain rates induced by the waviness, and termed this behaviour ‘oscillatory clustering’ (Marshall 2009; Hewitt & Marshall 2010). Nizkaya, Angilella & Buès (2014) neglected the lift force in analysing particle focusing in wavy channels. In light of these studies, one may question whether inertial lift force plays a critical role in particle focusing in wavy channels. Additionally, to the best of our knowledge, the variation of the inertial lift force has not been investigated in a wavy channel.

In this paper, we analytically and experimentally investigate the underlying mechanisms that drive focusing behaviour of neutrally buoyant particles in a wavy channel (figure 1). We provide a theoretical analysis for a particle that has an asymptotically small dimension compared with the channel width, as summarized in figure 2. To this end, we first calculate the flow in the wavy channel in the absence of particles, i.e. the particle-free flow or undisturbed flow. Throughout this paper, ‘disturbance/perturbation’ refers to the impact of particles on the particle-free flow. By incorporating the particle-free velocity field into the method of matched asymptotic analysis, we then calculate the inertial lift force on a neutrally buoyant particle in the wavy channel. We simulate the trajectory of the particle and predict focusing locations with a modified Maxey–Riley equation, incorporating source terms including the Stokes drag, fluid acceleration, added mass and lift force on the particle. We reveal the critical role of the inertial lift force in particle focusing and demonstrate different focusing behaviours than those observed in straight channels. By conducting experiments using particles that have finite dimensions compared with the channel width, we not only validate our predictions of the focusing locations but also reveal conditions in which realistic focusing behaviour deviates from the asymptotic analysis.

The paper is organized as follows: in § 2, we calculate the particle-free flow in the wavy channel. In § 3, we formulate the governing equations for the perturbations introduced by an asymptotically small neutrally buoyant particle. In § 4, we calculate the inertial lift force on the particle with matched asymptotic analysis. In § 5, we simulate the trajectory of the particle and predict its focusing locations. In § 6, we experimentally validate our predictions of the focusing locations, explore the focusing conditions and establish the differences in the focusing behaviour between wavy and straight channels. In § 7, we

Asymptotic theory ( $\epsilon \ll 1, \epsilon_w \ll 1, a/l \ll 1$ )

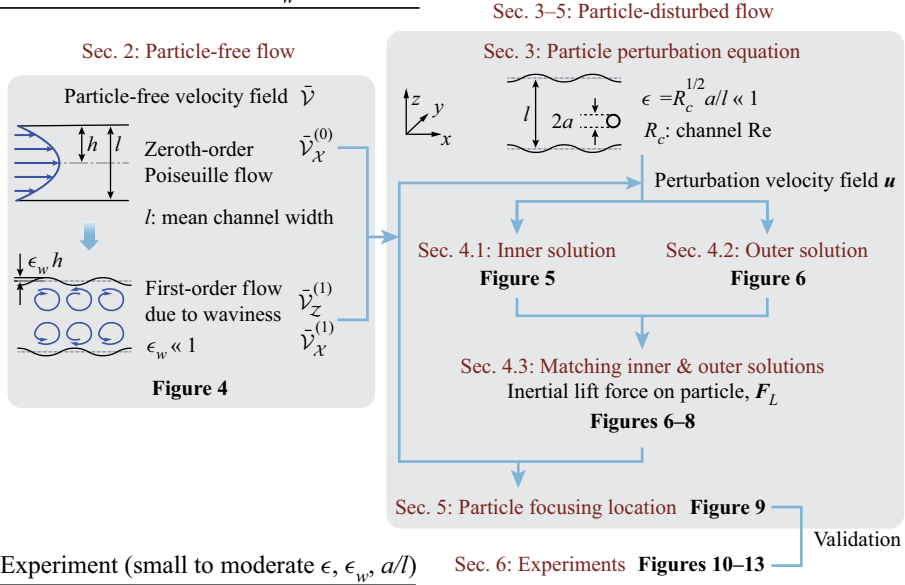


Figure 2. Structure of the paper. Throughout this work, perturbation refers to the impact of the particle on the particle-free flow.

introduce a scaling analysis to qualitatively compare the relative importance between the inertial lift and oscillatory straining effects, revealing how such competition leads to the variation of the focusing locations of particles in different parameter regimes.

### 2. Particle-free flow

We begin by computing the laminar particle-free velocity field in a two-dimensional wavy channel that extends infinitely in the out-of-plane direction. Consider fluid flow between two symmetric wavy plates with an average separation of  $l$ , as shown in figure 3. The wavy plates have a sinusoidal profile with amplitude  $\epsilon_w h$  and wavelength  $\lambda$ , where  $h$  is the mean half-width of the channel,  $h = l/2$ . We denote the angular frequency of the waviness as  $\omega'$ , i.e.  $\lambda = 2\pi/\omega'$ ; additionally, we assume  $\lambda$  is at least of  $O(h)$ . The laboratory frame is chosen with an origin located at the intersection between the middle plane and a cross-section on which the channel is of minimum width. We use the coordinate  $\mathcal{R}' = (\mathcal{X}', \mathcal{Y}', \mathcal{Z}')$  for the laboratory frame. The flow is driven by a pressure gradient in the  $\mathcal{X}'$  direction, and the velocity on the middle plane has an average magnitude of  $U'_m$ .

We non-dimensionalize our variables by normalizing the particle-free velocity  $\bar{\mathbf{V}}'$  with  $U'_m$  and by introducing  $\mathcal{R} = \mathcal{R}'/h = (\mathcal{X}, \mathcal{Y}, \mathcal{Z})$ . In the rest of the paper, dimensionless variables are indicated by a lack of primes. The particle-free fluid pressure  $\bar{P}'$  is normalized with  $\rho U'^2_m$ , where  $\rho$  is the fluid density. The dimensionless governing equations of  $\bar{\mathbf{V}}$  can then be written as the dimensionless Navier–Stokes equations and the continuity condition

$$\bar{\mathbf{v}} \cdot \nabla \bar{\mathbf{v}} = -\nabla \bar{p} + \frac{2}{R_c} \nabla^2 \bar{\mathbf{v}}, \tag{2.1a}$$

$$\nabla \cdot \bar{\mathbf{v}} = 0, \tag{2.1b}$$

Particle focusing in a wavy channel

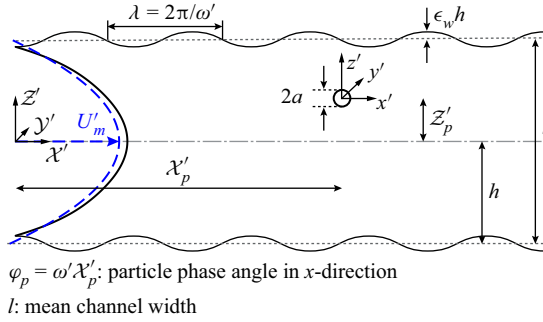


Figure 3. Schematics of the flow in a wavy channel and two sets of coordinate systems. The solid and dashed velocity profiles represent the actual flow at  $X' = 0$  and the zeroth-order plane Poiseuille flow, respectively.

where  $\bar{P}$  is the dimensionless particle-free fluid pressure,  $R_c = 2U'_m h/\nu$  is the channel Reynolds number (Schonberg & Hinch 1989; Hogg 1994; Asmolov 1999) and  $\nu$  is the kinematic viscosity of the fluid. The velocity  $\bar{\mathbf{V}}$  is subject to a no-slip boundary condition on the walls

$$\bar{\mathbf{V}} = 0 \quad \text{at } \mathcal{Z} = \pm 1 \mp \epsilon_w \text{Re}[\exp(i\omega\mathcal{X})], \quad (2.2)$$

where  $\omega = \omega' h$ . For a small waviness amplitude, i.e.  $\epsilon_w \ll 1$ , the particle-free velocity and pressure can be expressed as a series of higher-order corrections to Poiseuille flow

$$\bar{\mathbf{V}} = \bar{\mathbf{V}}^{(0)} + \epsilon_w \bar{\mathbf{V}}^{(1)} + O(\epsilon_w^2) \quad \text{and} \quad \bar{P} = \bar{P}^{(0)} + \epsilon_w \bar{P}^{(1)} + O(\epsilon_w^2), \quad (2.3a,b)$$

where the  $\mathcal{X}$ -component of the zeroth-order particle-free velocity is  $\bar{V}_x^{(0)} = 1 - \mathcal{Z}^2$ , the  $\mathcal{Z}$ -component of the zeroth-order particle-free velocity is  $\bar{V}_z^{(0)} = 0$  and the zeroth-order particle-free pressure  $\bar{P}^{(0)}$  varies linearly in the  $\mathcal{X}$  direction. Note that this expansion is distinct from the standard lubrication approach in which  $\epsilon_w h/\lambda \ll 1$ . Here, we instead allow for the case where the amplitude of the waviness may be of the same order as the wavelength.

To solve the first-order particle-free flow, we employ a strategy introduced by Van Dyke in 1975; instead of enforcing the no-slip condition at the wavy wall, we transfer the boundary condition in (2.2) to the average locations of the walls (Van Dyke 1975; Selvarajan, Tulapurkara & Vasanta Ram 1998, 1999) such that the no-slip condition is enforced at the wall to first order. To this end, we write (2.2) as a Taylor series around  $\mathcal{Z} = 1$  and then expand  $\bar{\mathbf{V}}$  and its derivatives in orders of  $\epsilon_w$  with (2.3a,b), finally arriving at

$$\bar{\mathbf{V}}_x^{(1)} \simeq \pm [\bar{\mathbf{V}}_x^{(0)}]' \text{Re}[\exp(i\omega\mathcal{X})] \quad \text{and} \quad (2.4a)$$

$$\bar{\mathbf{V}}_z^{(1)} \simeq \pm [\bar{\mathbf{V}}_z^{(0)}]' \text{Re}[\exp(i\omega\mathcal{X})] \quad \text{at } \mathcal{Z} = \pm 1, \quad (2.4b)$$

where the prime symbols denote derivatives with respect to  $\mathcal{Z}$ .

We now return to (2.1) to solve for the first-order velocity  $\bar{\mathbf{V}}^{(1)}$  and pressure  $\bar{P}^{(1)}$ . Inserting (2.3a,b) into (2.1) gives rise to the first-order governing equations, which are then solved with the transferred boundary condition (2.4). The first-order problem is linear in  $\bar{\mathbf{V}}^{(1)}$  and  $\bar{P}^{(1)}$ ; additionally,  $\mathcal{X}$  and  $\mathcal{Z}$  are separated in the transferred boundary conditions (2.4). Thus, we perform separation of variables and make the ansatz  $\bar{\mathbf{V}}^{(1)} = \text{Re}[\hat{\mathbf{V}}(\mathcal{Z}) \exp(i\omega\mathcal{X})]$  and  $\bar{P}^{(1)} = \text{Re}[\hat{P}(\mathcal{Z}) \exp(i\omega\mathcal{X})]$  following the structure of (2.4).

Herein,  $\hat{\mathcal{V}}(\mathcal{Z})$  and  $\hat{\mathcal{P}}(\mathcal{Z})$  are assumed to be complex functions, and the Re symbols ensure that the computed  $\bar{\mathcal{V}}^{(1)}$  and  $\bar{\mathcal{P}}^{(1)}$  are real-valued functions. The first-order variables  $\hat{\mathcal{V}}(\mathcal{Z})$  and  $\hat{\mathcal{P}}(\mathcal{Z})$  are then subject to the following differential equations and boundary conditions:

$$i\omega\hat{\mathcal{V}}_x + \frac{d\hat{\mathcal{V}}_z}{d\mathcal{Z}} = 0, \tag{2.5a}$$

$$i\omega(1 - \mathcal{Z}^2)\hat{\mathcal{V}}_x - 2\mathcal{Z}\hat{\mathcal{V}}_z = -i\omega\hat{\mathcal{P}} + \frac{2}{R_c} \left( -\omega^2 + \frac{d}{d\mathcal{Z}^2} \right) \hat{\mathcal{V}}_x, \tag{2.5b}$$

$$i\omega(1 - \mathcal{Z}^2)\hat{\mathcal{V}}_z = -\frac{d\hat{\mathcal{P}}}{d\mathcal{Z}} + \frac{2}{R_c} \left( -\omega^2 + \frac{d}{d\mathcal{Z}^2} \right) \hat{\mathcal{V}}_z, \tag{2.5c}$$

$$\hat{\mathcal{V}}_x = -2 \quad \text{and} \quad \hat{\mathcal{V}}_z = 0 \quad \text{at} \quad \mathcal{Z} = \pm 1. \tag{2.5d}$$

Note that we drop the Re symbols and the sinusoidal term  $\exp(i\omega\mathcal{X})$  in obtaining (2.5). Equation (2.5) can be solved numerically with the orthonormalization method (Conte 1966; Scott & Watts 1977). To avoid numerical instability, we perform integration from both boundaries and match the results at  $\mathcal{Z} = 0$ . In short, we solve (2.5) on two intervals,  $\mathcal{Z} \in [-1, 0]$  and  $\mathcal{Z} \in [0, 1]$ . For each interval, we write the solution as the summation of a particular solution and a linear combination of orthonormal homogeneous solutions, where the pre-factors for the homogeneous solutions are the unknowns. We integrate (2.5) from both boundaries  $\mathcal{Z} = \pm 1$ , and finally determine the pre-factors by utilizing the continuity of the functional values at  $\mathcal{Z} = 0$ .

Figure 4 shows the particle-free velocity field in a wavy channel. Unlike the zeroth-order flow which is independent of the  $\mathcal{X}$ -coordinate (figure 4a), the first-order velocity varies periodically along the  $\mathcal{X}$ -direction (figure 4b). Due to the waviness, a pair of counter-rotating vortices appear in both the  $\mathcal{X}$ - and  $\mathcal{Z}$ -directions in each period of the channel. To better illustrate the distributions of  $\bar{\mathcal{V}}_x^{(1)}$  and  $\bar{\mathcal{V}}_z^{(1)}$  across the channel, we select the cross-section  $\mathcal{X} = 0$  and show  $\bar{\mathcal{V}}_x^{(1)}(\mathcal{X} = 0)$  and  $\bar{\mathcal{V}}_z^{(1)}(\mathcal{X} = 0)$  as functions of  $\mathcal{Z}$  at varying channel Reynolds number  $R_c$  (figure 4c) and frequency  $\omega$  (figure 4d). The first-order  $x$ -velocity correction,  $\bar{\mathcal{V}}_x^{(1)}(\mathcal{X} = 0, \mathcal{Z})$  is symmetric about  $\mathcal{Z} = 0$ , whereas  $\bar{\mathcal{V}}_z^{(1)}(\mathcal{X} = 0, \mathcal{Z})$  is anti-symmetric. As  $R_c$  or  $\omega$  increases,  $\bar{\mathcal{V}}_x^{(1)}$  becomes more uniform, and the magnitude in the middle of the channel decreases; by contrast,  $\bar{\mathcal{V}}_x^{(1)}$  varies more sharply close to the boundaries. The magnitude of  $\bar{\mathcal{V}}_z^{(1)}$  does not vary monotonically with  $R_c$  (figure 4c). By contrast, the magnitude of  $\bar{\mathcal{V}}_z^{(1)}$  increases with  $\omega$  (figure 4d). The locations of the maximum and minimum  $\bar{\mathcal{V}}_z^{(1)}$  move toward the boundary of the channel as  $\omega$  increases. Figures 4(c) and 4(d) indicate that the shear rate close to the boundaries is positively related to  $R_c$  and  $\omega$ .

Figure 4 also includes the analytic solutions at the asymptotic limits  $R_c \rightarrow 0$  and  $\omega \rightarrow 0$  in 4(c) and 4(d), respectively. In the Stokes-flow limit, the first-order velocity component  $\bar{\mathcal{V}}_x^{(1)}(\mathcal{X} = 0, \mathcal{Z})$  is given by

$$\bar{\mathcal{V}}_x^{(1)}(\mathcal{X} = 0, \mathcal{Z}) = \frac{4 \cosh(\omega\mathcal{Z}) [-\omega \cosh(\omega) + \sinh(\omega)] + 4\omega\mathcal{Z} \sinh(\omega) \sinh(\omega\mathcal{Z})}{2\omega - \sinh(2\omega)}, \tag{2.6}$$

and  $\bar{\mathcal{V}}_z^{(1)}(\mathcal{X} = 0, \mathcal{Z})$  is calculated to be zero. As  $R_c$  decreases, our numerical computations asymptote to these analytic solutions, as shown in figure 4(c). In the limit of an

Particle focusing in a wavy channel

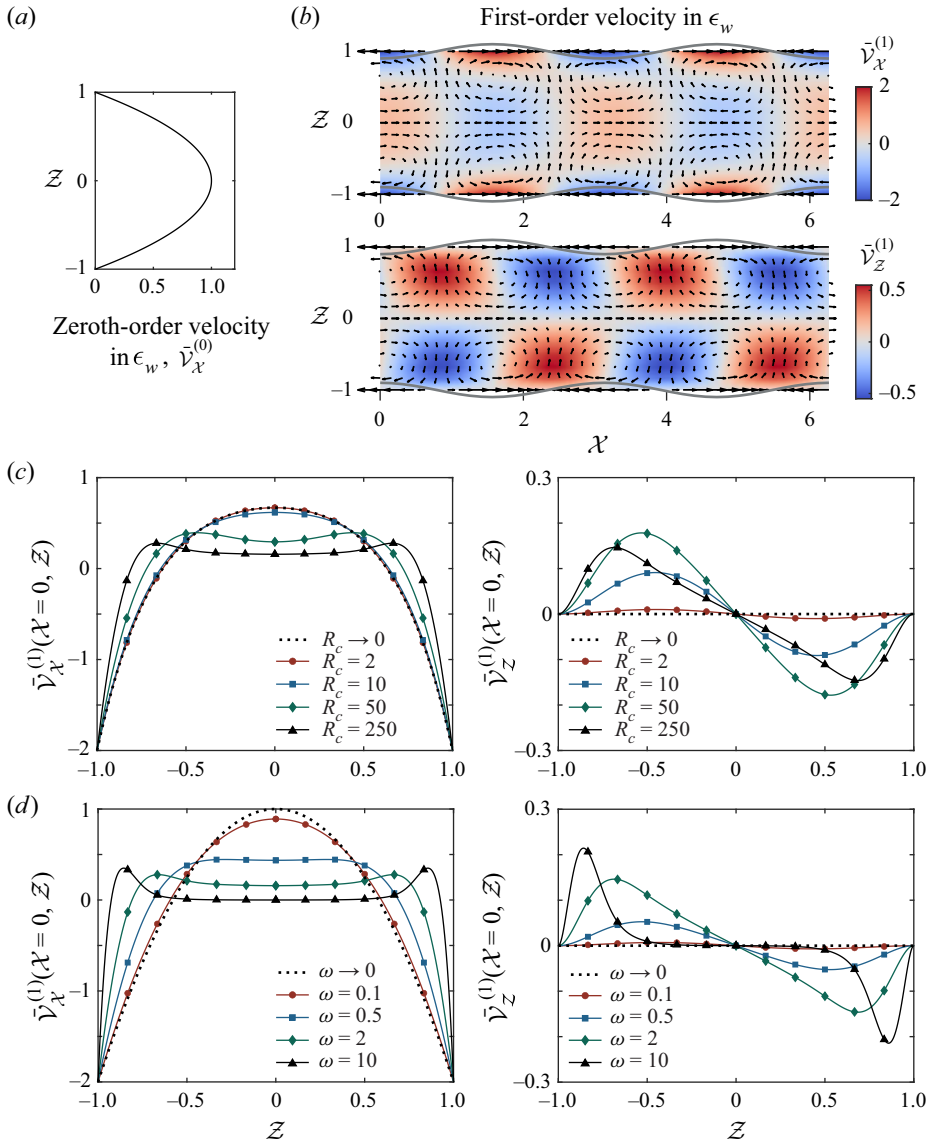


Figure 4. Particle-free flow in the wavy channel. The flow field can be approximated as the sum of (a) a zeroth-order Poiseuille flow  $\tilde{\mathbf{V}}^{(0)}$  and (b) a first-order flow  $\tilde{\mathbf{V}}^{(1)}$  which introduces eddies. In (b),  $R_c = 10$  and  $\omega = 2$ . (c) Variations of the first-order velocity components  $\tilde{v}_x^{(1)}$  and  $\tilde{v}_z^{(1)}$  across the channel at  $\mathcal{X} = 0$  for varying channel Reynolds numbers  $R_c$ , where  $\omega = 2$ . (d) Variations of the first-order velocity components  $\tilde{v}_x^{(1)}$  and  $\tilde{v}_z^{(1)}$  across the channel at  $\mathcal{X} = 0$  for varying frequencies  $\omega$  of the waviness, where  $R_c = 250$ . Dashed lines in (c,d) represent analytic solutions in the limits  $R_c \rightarrow 0$  and  $\omega \rightarrow 0$ , respectively.

infinitesimal waviness frequency, i.e.  $\omega \rightarrow 0$ , our numerical computations also asymptote to the analytic solutions (figure 4d), where

$$\tilde{v}_x^{(1)}(\mathcal{X} = 0, \mathcal{Z}) = 1 - 3\mathcal{Z}^2 \quad \text{and} \quad \tilde{v}_z^{(1)}(\mathcal{X} = 0, \mathcal{Z}) = 0. \quad (2.7a,b)$$

The detailed derivations for the Stokes-flow limit  $R_c \rightarrow 0$  and the lubrication limit  $\omega \rightarrow 0$  are reported in Appendices A and B.

### 3. Particle perturbation analysis formulation

We now introduce a spherical particle that gives rise to a perturbation to our particle-free channel flow. Hence, we investigate the perturbation in three dimensions. As shown in [figure 3](#), the particle is located at (dimensional) coordinates  $(\mathcal{X}'_p, \mathcal{Y}'_p, \mathcal{Z}'_p)$  and is moving with a (dimensional) translational velocity  $\mathbf{U}'_p = U'_{p,x}\mathbf{e}_x + U'_{p,z}\mathbf{e}_z$ , where  $\mathbf{e}_x$  and  $\mathbf{e}_z$  are unit vectors in the  $x$ - and  $z$ -directions, respectively. We define  $\varphi_p = \omega' \mathcal{X}'_p$  as the phase angle corresponding to the  $\mathcal{X}'$ -location of the particle ([figure 3](#)). To understand the perturbation induced by the particle, we choose a non-inertial frame of reference that is instantaneously located at the particle centre and translates at the particle velocity  $\mathbf{U}'_p$  (Hogg 1994; Asmolov 1999; Hood *et al.* 2015). Since the particle is free, the net force (including the virtual force due to the acceleration of the frame) acting on the particle is zero in this frame of reference. We use the coordinate  $\mathbf{r}' = (x', y', z')$  for the particle frame ([figure 3](#)). Let  $\bar{\mathbf{v}}'$  denote the particle-free velocity and  $\bar{p}'$  the particle-free pressure in the particle frame; namely, the velocity and pressure fields computed in the previous section are shifted by the (currently unknown) velocity  $\mathbf{U}'_p$ . The particle-free equations of motion can be written in terms of  $\bar{\mathbf{v}}'$  as

$$\rho \left( \frac{\partial \bar{\mathbf{v}}'}{\partial t'} + \bar{\mathbf{v}}' \cdot \nabla' \bar{\mathbf{v}}' + \mathbf{a}'_p \right) = -\nabla' \bar{p}' + \mu \nabla'^2 \bar{\mathbf{v}}', \tag{3.1a}$$

$$\nabla' \cdot \bar{\mathbf{v}}' = 0, \tag{3.1b}$$

$$\bar{\mathbf{v}}' = -\mathbf{U}'_p \quad \text{on the walls}, \tag{3.1c}$$

where  $\mathbf{a}'_p$  is the particle acceleration measured in the laboratory frame (Kundu, Cohen & Dowling 2016). Although (3.1) has been solved in the previous section, we rewrite it here in the particle frame as they will be used below to derive the governing equations for the difference between the disturbed and particle-free velocity fields.

We now consider the equations of motion for the flow field which is perturbed by the presence of the particle. Let  $\mathbf{v}'$  (note no overbar) denote the disturbed fluid velocity and  $p'$  the disturbed pressure in the particle frame. The equations for the disturbed flow take the same form of the Navier–Stokes equations and the continuity condition as (3.1)

$$\rho \left( \frac{\partial \mathbf{v}'}{\partial t'} + \mathbf{v}' \cdot \nabla' \mathbf{v}' + \mathbf{a}'_p \right) = -\nabla' p' + \mu \nabla'^2 \mathbf{v}', \tag{3.2a}$$

$$\nabla' \cdot \mathbf{v}' = 0. \tag{3.2b}$$

The boundary conditions include a no-slip boundary condition on the walls, a no-slip boundary condition on the surface of the particle and the absence of perturbation far away from the particle

$$\mathbf{v}' = -\mathbf{U}'_p \quad \text{on the walls}, \tag{3.3a}$$

$$\mathbf{v}' = \boldsymbol{\Omega}'_p \times \mathbf{r}' \quad \text{at } |\mathbf{r}'| = a, \tag{3.3b}$$

$$\mathbf{v}' = \bar{\mathbf{v}}' \quad \text{at } |x'| \rightarrow \infty, \tag{3.3c}$$

where  $a$  is the particle radius, and  $\boldsymbol{\Omega}'_p$  is the particle’s rotational velocity. Next, we define the perturbation velocity  $\mathbf{u}'$  as the difference between the disturbed and the particle-free velocities, i.e.  $\mathbf{u}' = \mathbf{v}' - \bar{\mathbf{v}}'$ . The governing equations of  $\mathbf{u}'$  can be obtained by subtracting



(3.1) from (3.2)

$$\frac{\partial \mathbf{u}'}{\partial t'} + \mathbf{u}' \cdot \nabla' \mathbf{u}' + \bar{\mathbf{v}}' \cdot \nabla' \mathbf{u}' + \mathbf{u}' \cdot \nabla' \bar{\mathbf{v}}' = -\frac{1}{\rho} \nabla' (p' - \bar{p}') + \nu \nabla'^2 \mathbf{u}', \quad (3.4a)$$

$$\nabla' \cdot \mathbf{u}' = 0. \quad (3.4b)$$

Note that the particle acceleration  $\mathbf{a}'_p$  in (3.1) and (3.2) cancels out during subtraction. The boundary conditions of (3.4) are

$$\mathbf{u}' = 0 \quad \text{at } z' = \begin{cases} -Z'_p - h + \epsilon_w h \operatorname{Re}\{\exp[i(\omega'x' + \varphi_p)]\} \\ h - Z'_p - \epsilon_w h \operatorname{Re}\{\exp[i(\omega'x' + \varphi_p)]\} \end{cases}, \quad (3.5a)$$

$$\mathbf{u}' = \boldsymbol{\Omega}'_p \times \mathbf{r}' - \bar{\mathbf{v}}' \quad \text{at } |\mathbf{r}'| = a, \quad (3.5b)$$

$$\mathbf{u}' = \mathbf{0} \quad \text{at } |x'| \rightarrow \infty. \quad (3.5c)$$

We non-dimensionalize (3.5) by introducing

$$\left. \begin{aligned} \mathbf{r} &= \frac{\mathbf{r}'}{a}, \quad \mathbf{u} = \frac{\mathbf{u}'}{U'_m}, \quad \bar{\mathbf{v}} = \frac{\bar{\mathbf{v}}'}{U'_m}, \quad \omega = \omega' h, \\ \boldsymbol{\Omega}_p &= \frac{2h\boldsymbol{\Omega}'_p}{U'_m}, \quad \text{and} \quad q = \left(\frac{\mu U'_m}{a}\right)^{-1} (p' - \bar{p}'), \end{aligned} \right\} \quad (3.6)$$

where  $\bar{\mathbf{v}}$  is the dimensionless particle-free velocity in the particle frame,  $q$  is the dimensionless perturbation pressure and a lack of prime denotes dimensionless variables. Additionally, we introduce a particle Reynolds number  $R_p = U'_m a^2 / (\nu)$  (Schonberg & Hinch 1989; Hogg 1994; Asmolov 1999), where  $\nu$  is the kinematic viscosity of the fluid. We define  $\epsilon = R_p^{1/2} = R_c^{1/2} a / l$  (Asmolov 1999; Matas *et al.* 2009). This small dimensionless parameter  $\epsilon$  is taken to be the asymptotic parameter that we will use to analyse the perturbation introduced by the particle, and we assume  $\epsilon \ll 1$ . Hence, we have the following dimensionless governing equations of  $\mathbf{u}$ :

$$\epsilon R_c^{1/2} \left( \frac{\partial \mathbf{u}}{\partial t} + \mathbf{u} \cdot \nabla \mathbf{u} + \bar{\mathbf{v}} \cdot \nabla \mathbf{u} + \mathbf{u} \cdot \nabla \bar{\mathbf{v}} \right) = -\nabla q + \nabla^2 \mathbf{u}, \quad (3.7a)$$

$$\nabla \cdot \mathbf{u} = 0, \quad (3.7b)$$

with boundary conditions

$$\mathbf{u} = \mathbf{0} \quad \text{at } z = \frac{1}{2} \epsilon^{-1} R_c^{1/2} (\mp 1 - Z_p \pm \epsilon_w \operatorname{Re}\{\exp[i(\varphi_p + x\epsilon\kappa)]\}), \quad (3.8a)$$

$$\mathbf{u} = \epsilon R_c^{-1/2} \boldsymbol{\Omega}_p \times \mathbf{r} - \bar{\mathbf{v}} \quad \text{at } |\mathbf{r}| = 1, \quad (3.8b)$$

$$\mathbf{u} = \mathbf{0} \quad \text{at } |x| \rightarrow \infty, \quad (3.8c)$$

where we replace  $2\omega R_c^{-1/2}$  with  $\kappa$ , and  $\bar{\mathbf{v}}$  is the non-dimensional particle-free flow field in the frame of the particle. Additionally, we factor out  $\epsilon$  in the exponential term of (3.8a) for mathematical convenience in § 4.2.

Finally, we express the particle-frame-based particle-free velocity  $\bar{\mathbf{v}}$  in (3.7) using quantities that have been calculated in § 2. In terms of the dimensionless particle-free

velocity  $\bar{\mathbf{V}}$  in the laboratory frame, and the dimensionless particle velocity  $U_p$  we have

$$\bar{\mathbf{v}} = \bar{\mathbf{V}} - U_p. \tag{3.9}$$

We further rewrite the arguments of  $\bar{\mathbf{V}}$ ,  $\bar{\mathbf{V}}^{(0)}$ ,  $\bar{\mathbf{V}}^{(1)}$  and  $\hat{\mathbf{V}}$  in terms of the dimensionless coordinates in the particle frame  $x$ ,  $y$  and  $z$  with the relationships  $\mathcal{X} = ax/h + \mathcal{X}_p$  and  $\mathcal{Z} = az/h + \mathcal{Z}_p$ , e.g.  $\hat{V}_x(\mathcal{Z}) = \hat{V}_x(2\epsilon z R_c^{-1/2} + \mathcal{Z}_p)$ . Note that a conversion between  $\mathcal{Y}$  and  $y$  is not necessary because the  $y$ -components of both  $\bar{\mathbf{V}}$  and  $U_p$  are equal to zero, leading to  $\bar{v}_y = 0$  (3.9); similarly, all  $y$ -components in the rest of this section vanish. Moreover, since the perturbation velocity  $\mathbf{u}$  is influenced by the lag between the particle velocity  $U_p$  and the particle-free velocity at the instantaneous location of the particle centre  $\bar{\mathbf{V}}(\mathcal{R}_p(t))$ , we define a dimensionless particle slip velocity,  $V_s = \bar{\mathbf{V}}(\mathcal{R}_p(t)) - U_p$ . Inserting (2.3a,b), the asymptotic expansions for  $\bar{\mathbf{V}}$  and  $\bar{P}$  into (3.9), we find

$$\bar{v}_x = V_{s,x} + \Delta\bar{V}_x^{(0)} + \epsilon_w \Delta\bar{V}_x^{(1)} + O(\epsilon_w^2), \quad \bar{v}_z = V_{s,z} + \epsilon_w \Delta\bar{V}_z^{(1)} + O(\epsilon_w^2), \tag{3.10a,b}$$

where  $\Delta\bar{V}_x^{(i)}$  represents the difference between the  $i$ th order particle-free velocity at location  $\mathbf{r} = (x, y, z)$  and the  $i$ th-order particle-free velocity at the particle centre  $(0, 0, 0)$ . Here,  $\Delta\bar{V}_x^{(0)} = \epsilon \gamma z R_c^{-1/2} - 4\epsilon^2 z^2 R_c^{-1}$  and  $\Delta\bar{V}_z^{(0)} = 0$ , where  $\gamma = -4\mathcal{Z}_p$  is the zeroth-order shear rate at the particle centre normalized with a characteristic shear rate,  $U'_m/l$ . Additionally,

$$\Delta\bar{V}_x^{(1)} = \text{Re}\{\hat{V}_x(2\epsilon z R_c^{-1/2} + \mathcal{Z}_p) \exp[i(\varphi_p + \epsilon x \kappa)] - \hat{V}_x(\mathcal{Z}_p) \exp(i\varphi_p)\}, \tag{3.11a}$$

$$\Delta\bar{V}_z^{(1)} = \text{Re}\{\hat{V}_z(2\epsilon z R_c^{-1/2} + \mathcal{Z}_p) \exp[i(\varphi_p + \epsilon x \kappa)] - \hat{V}_z(\mathcal{Z}_p) \exp(i\varphi_p)\}. \tag{3.11b}$$

To determine the orders of  $\Delta\bar{V}_x^{(1)}$  and  $\Delta\bar{V}_z^{(1)}$  in  $\epsilon$  for later analyses in § 4, we first write the Taylor series expansions of  $\hat{V}_x(2\epsilon z R_c^{-1/2} + \mathcal{Z}_p)$  and  $\hat{V}_z(2\epsilon z R_c^{-1/2} + \mathcal{Z}_p)$  at  $z = 0$  under the condition  $2\epsilon z R_c^{-1/2} \ll 1$

$$\hat{V}_x(2\epsilon z R_c^{-1/2} + \mathcal{Z}_p) = \hat{V}_{x0} + \alpha_x \epsilon z R_c^{-1/2} + \frac{1}{2} \beta_x \epsilon^2 z^2 R_c^{-1} + O(\epsilon^3), \tag{3.12a}$$

$$\hat{V}_z(2\epsilon z R_c^{-1/2} + \mathcal{Z}_p) = \hat{V}_{z0} + \alpha_z \epsilon z R_c^{-1/2} + \frac{1}{2} \beta_z \epsilon^2 z^2 R_c^{-1} + O(\epsilon^3), \tag{3.12b}$$

where  $\hat{V}_{x0} = \hat{V}_x(\mathcal{Z}_p)$ ,  $\hat{V}_{z0} = \hat{V}_z(\mathcal{Z}_p)$  and  $\alpha_x$ ,  $\alpha_z$ ,  $\beta_x$  and  $\beta_z$  are prefactors of the Taylor series, which can be determined numerically from the solutions to (2.5). Specifically, the continuity condition gives rise to the relation  $i\kappa R_c^{1/2} \hat{V}_{x0} + \alpha_z = 0$ . Given (3.12), we further expand  $\Delta\bar{V}_x^{(1)}$  and  $\Delta\bar{V}_z^{(1)}$  in Taylor series with respect to both  $x$  and  $z$ , and find that  $\Delta\bar{V}_x^{(1)}$  and  $\Delta\bar{V}_z^{(1)}$  are of  $O(\epsilon)$ , e.g.  $\Delta\bar{V}_x^{(1)} = \text{Re}[(i\kappa \hat{V}_{x0} + \alpha_x z R_c^{-1/2}) \exp(i\varphi_p)] \epsilon + O(\epsilon^2)$ . These expressions will be used to express the boundary conditions order by order at the surface of a particle in the following section. Furthermore, we can analytically obtain the variables in (3.11) and (3.12) in the lubrication limit where the angular frequency  $\omega \rightarrow 0$  (Appendix B)

$$\Delta\bar{V}_x^{(1)} \rightarrow -12z\epsilon(\mathcal{Z}_p R_c^{-1/2} + z\epsilon R_c^{-1}) \cos(\varphi_p) \quad \text{and} \quad \Delta\bar{V}_z^{(1)} \rightarrow 0, \tag{3.13a,b}$$

which are of  $O(\epsilon)$ . We further find in this limit:  $\hat{V}_{x0} \rightarrow 1 - 3\mathcal{Z}_p^2$ ,  $\hat{V}_{z0} \rightarrow 0$ ,  $\alpha_x \rightarrow -12\mathcal{Z}_p$ ,  $\alpha_z \rightarrow 0$ ,  $\beta_x \rightarrow -24$  and  $\beta_z \rightarrow 0$ .

#### 4. Inertial lift force acting on a neutrally buoyant particle

The particle induces a small perturbation to the steady channel flow and hence experiences an inertial lift force in the lateral direction. In this section, we calculate the inertial lift force on a neutrally buoyant particle (recall that we seek to determine whether particle focusing in wavy channels arises from this lift force). The problem formulated in (3.7) is solved with the method of matched asymptotic expansions (Schonberg & Hinch 1989; Hogg 1994; Asmolov 1999). We first solve an inner problem to obtain the flow field surrounding the particle. We then regard the particle as a singular point that exerts a force on the channel flow in an outer problem. Finally, matching the inner and outer solutions gives rise to a lift force on the particle.

##### 4.1. Inner solution

We introduce an inner expansion of the perturbation velocity and pressure

$$\mathbf{u} = \mathbf{u}_0 + \epsilon \mathbf{u}_1 + O(\epsilon^2), \quad q = q_0 + \epsilon q_1 + O(\epsilon^2). \quad (4.1a,b)$$

Inserting (4.1a,b) into (3.7), the zeroth-order governing equations represent a Stokes-flow problem

$$\nabla^2 \mathbf{u}_0 - \nabla q_0 = \mathbf{0}, \quad (4.2a)$$

$$\nabla \cdot \mathbf{u}_0 = 0, \quad (4.2b)$$

$$\mathbf{u}_0 = -V_{s,x} \mathbf{e}_x - V_{s,z} \mathbf{e}_z, \quad |\mathbf{r}| = 1, \quad (4.2c)$$

$$\mathbf{u}_0 \rightarrow \mathbf{0}, \quad \mathbf{r} \rightarrow \infty. \quad (4.2d)$$

In the absence of fluid inertia, we apply Faxén’s law and find that  $V_{s,x}$  and  $V_{s,z}$  are of  $O(\epsilon^2 R_c^{-1})$ . Thus, (4.2c) reduces to  $\mathbf{u}_0 = \mathbf{0}$  on the particle surface, and  $\mathbf{u}_0$  vanishes everywhere in the channel. The first-order governing equations are then

$$\nabla^2 \mathbf{u}_1 - \nabla q_1 = \mathbf{0}, \quad (4.3a)$$

$$\nabla \cdot \mathbf{u}_1 = 0, \quad (4.3b)$$

$$\mathbf{u}_1 = R_c^{-1/2} (\boldsymbol{\Omega}_p \times \mathbf{r} - \gamma z \mathbf{e}_x) - \epsilon_w \epsilon^{-1} \Delta \bar{\mathcal{V}}_x^{(1)} \mathbf{e}_x - \epsilon_w \epsilon^{-1} \Delta \bar{\mathcal{V}}_z^{(1)} \mathbf{e}_z, \quad |\mathbf{r}| = 1, \quad (4.3c)$$

$$\mathbf{u}_1 \rightarrow \mathbf{0}, \quad \mathbf{r} \rightarrow \infty, \quad (4.3d)$$

where both  $\epsilon^{-1} \Delta \bar{\mathcal{V}}_x^{(1)}$  and  $\epsilon^{-1} \Delta \bar{\mathcal{V}}_z^{(1)}$  are of  $O(1)$  (see the end of §3). We also assume that  $\epsilon_w$  and  $\epsilon$  are of the same order of magnitude such that the last two terms in (4.3c) are bounded. The first-order problem is still a Stokes-flow problem. Due to its linearity, (4.3) can be decomposed into several sub-problems, which we solve separately based on the fundamental solutions for a sphere immersed in Stokes flow derived by Guazzelli & Morris (2011). For a rotational boundary condition with dimensionless rotation rate  $\boldsymbol{\omega}$  at the particle surface, i.e.  $\mathbf{u}_1 = \boldsymbol{\omega} \times \mathbf{r}$  at  $|\mathbf{r}| = 1$ , the perturbation velocity  $\mathbf{u}_1$  is given by

$$\mathbf{u}_1 = \boldsymbol{\omega} \times \frac{\mathbf{r}}{r^3}, \quad (4.4)$$

which is adapted from (2.7) in Guazzelli & Morris (2011). For a straining boundary condition with dimensionless strain-rate tensor  $\mathbf{E}$  at the particle surface, i.e.  $\mathbf{u}_1 = \mathbf{E} \mathbf{r}$  at

$|\mathbf{r}| = 1$ , the components of the perturbation velocity  $\mathbf{u}_1$  are given by

$$u_{1i} = \frac{5}{2} \frac{x_i (x_j E_{jk} x_k)}{r^5} + \frac{1}{2} E_{jk} \left[ \frac{\delta_{ij} x_k + \delta_{ik} x_j}{r^5} - \frac{5 x_i x_j x_k}{r^7} \right], \tag{4.5}$$

which is adapted from (2.17) in Guazzelli & Morris (2011). Based on these fundamental solutions, we decompose  $\mathbf{u}_1(\mathbf{r})$  into three parts:  $\mathbf{u}_1(\mathbf{r}) = \mathbf{u}_{1A}(\mathbf{r}) + \mathbf{u}_{1B}(\mathbf{r}) + \mathbf{u}_{1C}(\mathbf{r})$  to satisfy the different components in boundary condition (4.3c). In (4.3c), the term  $R_c^{-1/2} (\boldsymbol{\Omega}_p \times \mathbf{r})$  at the boundary corresponds to a pure rotational boundary condition with a dimensionless rotation rate  $\boldsymbol{\omega} = R_c^{-1/2} \boldsymbol{\Omega}_p$ , which gives rise to the solution

$$\mathbf{u}_{1A}(\mathbf{r}) = R_c^{-1/2} \boldsymbol{\Omega}_p \times \frac{\mathbf{r}}{r^3}. \tag{4.6}$$

The term  $-R_c^{-1/2} \gamma z \mathbf{e}_x$  in (4.3c) represents a simple-shear boundary condition, which can be treated as the combination of a rotational boundary condition with a dimensionless rotation rate  $\boldsymbol{\omega} = -R_c^{-1/2} (\gamma/2) \mathbf{e}_y$  and a straining boundary condition with a dimensionless strain-rate tensor

$$\mathbf{E} = -\frac{1}{2} R_c^{-1/2} \begin{bmatrix} 0 & 0 & \gamma \\ 0 & 0 & 0 \\ \gamma & 0 & 0 \end{bmatrix}. \tag{4.7}$$

We then construct the following solution:

$$\mathbf{u}_{1B}(\mathbf{r}) = R_c^{-1/2} \left[ -\frac{\gamma}{2} \mathbf{e}_y \times \frac{\mathbf{r}}{r^3} + \frac{5}{2} \gamma r x z \left( \frac{1}{r^7} - \frac{1}{r^5} \right) - \frac{\gamma}{2 r^5} (\mathbf{e}_x z + \mathbf{e}_z x) \right]. \tag{4.8}$$

The terms  $-\epsilon_w \epsilon^{-1} \Delta \bar{\mathcal{V}}_x^{(1)} \mathbf{e}_x - \epsilon_w \epsilon^{-1} \Delta \bar{\mathcal{V}}_z^{(1)} \mathbf{e}_z$  in (4.3c) can be treated as the combination of a rotational and a straining boundary condition. Given (3.11), we find the Taylor series for these two terms at the origin and only collect the leading-order terms in  $\epsilon$ . The corresponding strain-rate tensor  $\mathbf{E}$  and rotation vector  $\boldsymbol{\omega}$  at the origin can be written as

$$\left. \begin{aligned} \mathbf{E} &= -\epsilon_w R_c^{-1/2} \operatorname{Re} \left\{ \exp(i\varphi_p) \begin{bmatrix} -\alpha_z & 0 & \frac{\zeta}{2} \\ 0 & 0 & 0 \\ \frac{\zeta}{2} & 0 & \alpha_z \end{bmatrix} \right\} \\ &\quad \text{and} \\ \boldsymbol{\omega} &= -\epsilon_w R_c^{-1/2} \operatorname{Re} \left\{ \exp(i\varphi_p) \begin{bmatrix} 0 \\ \sigma \\ 0 \end{bmatrix} \right\}, \end{aligned} \right\} \tag{4.9}$$

where  $\zeta := \alpha_x + i\kappa R_c^{1/2} \hat{\mathcal{V}}_{z0}$  and  $\sigma := \alpha_x - i\kappa R_c^{1/2} \hat{\mathcal{V}}_{z0}$ , which reduces to  $\zeta = \sigma = -12\mathcal{Z}_p$  for an infinitesimal angular frequency  $\omega$ . The third component of the first-order velocity

field  $\mathbf{u}_{1C}(\mathbf{r})$  is thus given by

$$\mathbf{u}_{1C}(\mathbf{r}) = \epsilon_w R_c^{-1/2} \operatorname{Re} \left\{ \exp(i\varphi_p) \left[ \left( -\frac{\sigma}{2} \mathbf{e}_y \right) \times \frac{\mathbf{r}}{r^3} + \frac{5}{2} \mathbf{r} \left( \zeta xz - \alpha_z x^2 + \alpha_z z^2 \right) \left( \frac{1}{r^7} - \frac{1}{r^5} \right) - \frac{\zeta}{2} \left( \frac{z\mathbf{e}_x + x\mathbf{e}_z}{r^5} \right) + \alpha_z \left( \frac{x\mathbf{e}_x - z\mathbf{e}_z}{r^5} \right) \right] \right\}. \quad (4.10)$$

We now determine the rotation velocity  $\boldsymbol{\Omega}_p$  by establishing the balance of moment on the particle. According to Faxén’s second law, the leading-order dimensional hydrodynamic torque on the particle  $\mathbf{T}'$  is proportional to the relative rotation velocity between the undisturbed flow and the particle (Guazzelli & Morris 2011)

$$\mathbf{T}' = 8\pi\mu a^3 (\bar{\boldsymbol{\Omega}}'(\mathbf{r}' = \mathbf{0}) - \boldsymbol{\Omega}'_p), \quad (4.11)$$

where  $\bar{\boldsymbol{\Omega}}'(\mathbf{r}' = \mathbf{0}) = \nabla' \times \bar{\mathbf{v}}'/2$  is the rotation vector of the undisturbed flow evaluated at the particle centre. The torque leads to the angular acceleration of the particle, i.e.  $\mathbf{T}' = I_p d\boldsymbol{\Omega}'_p/dt'$ , where  $I_p = (2/5)a^2 m_p$  is the moment of inertia of the particle. Since we assume that the wavelength of the channel  $\lambda$  is at least of  $O(l)$ , the characteristic time scale  $t'$  for the variation of  $\boldsymbol{\Omega}'_p$  is taken to be  $l/U'_m$ . Further normalizing the rotation vectors with  $U'_m/l$  (3.6), we can establish the following moment balance on the neutrally buoyant particle:

$$\frac{1}{15} \epsilon^2 \frac{d\boldsymbol{\Omega}_p}{dt} = \bar{\boldsymbol{\Omega}}(\mathbf{r} = \mathbf{0}) - \boldsymbol{\Omega}_p. \quad (4.12)$$

Expanding  $\boldsymbol{\Omega}_p$  into orders of  $\epsilon$ , we find  $\boldsymbol{\Omega}_p^{(0)} = \bar{\boldsymbol{\Omega}}(\mathbf{r} = \mathbf{0})$ . Namely, in the framework of the first-order perturbation analysis in  $\epsilon$ , the particle follows the rotation of the undisturbed flow at the instantaneous particle centre, exerting no net hydrodynamic torque on the fluid. Therefore, the summation of all rotational components in  $\mathbf{u}_1(\mathbf{r})$  must vanish, and  $\boldsymbol{\Omega}_p^{(0)}$  equals  $\{\gamma + \epsilon_w \operatorname{Re}[\exp(i\varphi_p)\sigma]\} \mathbf{e}_y/2$ . Instead of a lift force, the perturbation velocity  $\mathbf{u}_1(\mathbf{r})$  leads to a strainlet (or force dipole) on the particle. The truncated term  $\boldsymbol{\Omega}_p - \boldsymbol{\Omega}_p^{(0)}$  generates a rotlet, but its strength is negligible compared with the strainlet. To give a sense of the perturbation velocity field associated with the strainlet, figure 5 shows the distributions of the  $x$  and  $z$  components of  $\mathbf{u}_1(\mathbf{r})$  on the plane  $y = 0$  in the particle frame. Furthermore, at the limit  $\epsilon_w \rightarrow 0$ , our analytic expression of  $\mathbf{u}_1(\mathbf{r})$  recovers the corresponding expression in a straight channel (see (5.3) in Asmolov 1999).

#### 4.2. Outer solution

To find the lift force, we now turn to the outer region in which the balance between the viscous and inertial effects are important. In the outer problem, we introduce outer coordinates  $\mathbf{R} = (X, Y, Z)$  that are related to the inner variables via  $\mathbf{R} = \epsilon \mathbf{r}$ . The perturbation velocity and pressure fields are then expressed as  $\mathbf{U}(\mathbf{R})$  and  $P(\mathbf{R})$ , respectively.

To match the inner and outer problems, we regard the particle as a singular point that exerts a strainlet on the flow field. We will introduce the strainlet as a forcing term at the origin in the momentum equations of the outer problem. To this end, we first convert  $\mathbf{u}_1(\mathbf{r})$

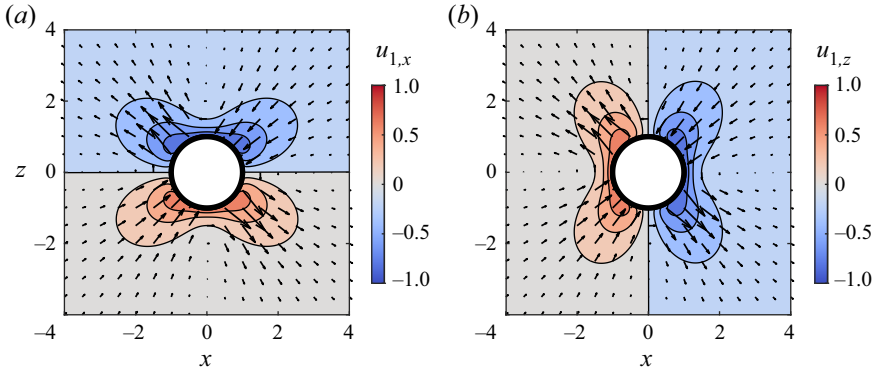


Figure 5. Distributions of the (a)  $x$ -component and (b)  $z$ -component of the first-order perturbation velocity  $\mathbf{u}_1(\mathbf{r})$  on the plane  $y = 0$ , where  $\mathbf{r} = (x, y, z)$  denotes the coordinate system in the particle frame. Arrows represent the vector field  $\mathbf{u}_1(\mathbf{r})$ , and the circle represents the particle surface. In this example,  $R_c = 100$ ,  $\omega = 2$ ,  $Z_p = 0.5$ ,  $\varphi_p = 0.3$  and  $\epsilon_w = 0.05$ .

(see (4.6)–(4.10)) to a function of outer coordinates

$$\mathbf{u}_1(\mathbf{R}) = \frac{5}{2} \epsilon^2 R_c^{-1/2} \frac{\mathbf{R}}{R^5} \{-\gamma XZ + \epsilon_w \text{Re}[\exp(i\varphi_p)(-\zeta XZ + \alpha_z X^2 - \alpha_z Z^2)]\} + O(\epsilon^4). \tag{4.13}$$

Given (4.1a,b) and (4.13), we now propose an outer expansion of the perturbation field

$$\mathbf{u} = \epsilon^3 \mathbf{U} + O(\epsilon^4), \quad q = \epsilon^4 Q + O(\epsilon^5). \tag{4.14a,b}$$

For a general strain tensor  $\mathbf{E}$  and the corresponding strainlet velocity field  $\mathbf{u} = 5x_i E_{ij} x_j \mathbf{r} / (2r^5)$ , the singular forcing term on the right-hand side of the outer momentum equations takes the form of  $20\pi E_{ij} \partial \delta(\mathbf{r}) / \partial x_j$  (Hogg 1994). Hence, the governing equations and boundary conditions for our outer problem are

$$\begin{aligned} R_c^{\frac{1}{2}} (\bar{\mathbf{v}} \cdot \nabla \mathbf{U} + \mathbf{U} \cdot \nabla \bar{\mathbf{v}}) &= \nabla Q + \nabla^2 \mathbf{U} - \frac{10}{3} \pi R_c^{-1/2} \gamma \left[ \frac{\partial \delta(\mathbf{R})}{\partial Z} \mathbf{e}_x + \frac{\partial \delta(\mathbf{R})}{\partial X} \mathbf{e}_z \right] \\ &+ \epsilon_w \frac{10}{3} \pi R_c^{-1/2} \text{Re} \left[ \exp(i\varphi_p) \left\{ -\zeta \left[ \frac{\partial \delta(\mathbf{R})}{\partial Z} \mathbf{e}_x + \frac{\partial \delta(\mathbf{R})}{\partial X} \mathbf{e}_z \right] \right. \right. \\ &\left. \left. + 2\alpha_z \left[ \frac{\partial \delta(\mathbf{R})}{\partial X} \mathbf{e}_x - \frac{\partial \delta(\mathbf{R})}{\partial Z} \mathbf{e}_z \right] \right\} \right] \end{aligned} \tag{4.15a}$$

$$\nabla \cdot \mathbf{U} = 0 \tag{4.15b}$$

$$\mathbf{U} = \mathbf{0} \quad \text{at } Z = \frac{1}{2} R_c^{1/2} (\mp 1 - Z_p \pm \epsilon_w \text{Re}\{\exp[i(\varphi_p + X\kappa)]\}). \tag{4.15c}$$

In obtaining (4.15a), we neglect the time-derivative term. This is because the time scale for the establishment of the disturbance flow,  $l^2/\nu$ , is much smaller than the time scale over which the particle migrates laterally relative to the particle-free flow,  $l/U_{lateral}$  (Hogg 1994). Here,  $U_{lateral}$  denotes the lateral migration velocity of the particle. We also neglect a term  $\epsilon^3 \mathbf{U} \cdot \nabla \mathbf{U}$  in (4.15a), as the interaction of the perturbation flow with itself is

negligible compared with other inertial terms. Next, we expand  $R_c^{1/2}\bar{\mathbf{v}}$ ,  $U$ , and  $Q$  in powers of  $\epsilon_w$

$$R_c^{1/2}\bar{v}_x = \bar{V}_x^{(0)} + \epsilon_w \bar{V}_x^{(1)} + O(\epsilon_w^2), \quad R_c^{1/2}\bar{v}_z = \epsilon_w \bar{V}_z^{(1)} + O(\epsilon_w^2), \quad (4.16a)$$

$$U = U^{(0)} + \epsilon_w U^{(1)} + O(\epsilon_w^2), \quad Q = Q^{(0)} + \epsilon_w Q^{(1)} + O(\epsilon_w^2), \quad (4.16b)$$

where  $\bar{V}_x^{(0)} = \gamma Z - 4Z^2 R_c^{-1/2}$ ,  $\bar{V}_x^{(1)} = R_c^{1/2} \Delta \bar{V}_x^{(1)}$  and  $\bar{V}_z^{(1)} = R_c^{1/2} \Delta \bar{V}_z^{(1)}$  (3.10a,b), which reduce to  $\bar{V}_x^{(1)} \rightarrow -12z\epsilon(\mathcal{Z}_p + z\epsilon R_c^{-1/2}) \cos(\varphi_p)$  and  $\bar{V}_z^{(1)} \rightarrow 0$  in the limit  $\omega \rightarrow 0$ . Expanding (4.15) and collecting like terms in  $\epsilon_w$ , we obtain the zeroth-order governing equations and boundary conditions

$$\begin{aligned} \nabla^2 U^{(0)} - \nabla Q^{(0)} - \bar{V}_x^{(0)} \frac{\partial U^{(0)}}{\partial X} - U_z^{(0)} \frac{d\bar{V}_x^{(0)}}{dZ} \mathbf{e}_x \\ = -\frac{10}{3} \pi R_c^{-1/2} \gamma \left[ \frac{\partial \delta(\mathbf{R})}{\partial Z} \mathbf{e}_x + \frac{\partial \delta(\mathbf{R})}{\partial X} \mathbf{e}_z \right], \end{aligned} \quad (4.17a)$$

$$\nabla \cdot U^{(0)} = 0, \quad (4.17b)$$

$$U^{(0)} = \mathbf{0}, \quad \text{at } Z_- = -\frac{1}{2} R_c^{1/2} (1 + \mathcal{Z}_p) \quad \text{and} \quad Z_+ = \frac{1}{2} R_c^{1/2} (1 - \mathcal{Z}_p), \quad (4.17c)$$

$$U^{(0)} = \mathbf{0}, \quad X \rightarrow \infty, \quad (4.17d)$$

where  $Z_-$  and  $Z_+$  denote the  $Z$ -coordinates of the average locations of the walls. The first-order governing equations in  $\epsilon_w$  take the form

$$\begin{aligned} \nabla^2 U^{(1)} - \nabla Q^{(1)} - \bar{V}_x^{(0)} \frac{\partial U^{(1)}}{\partial X} - U_z^{(1)} \frac{d\bar{V}_x^{(0)}}{dZ} \mathbf{e}_x = \bar{V}_x^{(1)} \frac{\partial U^{(0)}}{\partial X} + \bar{V}_z^{(1)} \frac{\partial U^{(0)}}{\partial Z} \\ + \left( U_x^{(0)} \frac{\partial \bar{V}_x^{(1)}}{\partial X} + U_z^{(0)} \frac{\partial \bar{V}_x^{(1)}}{\partial Z} \right) \mathbf{e}_x + \left( U_x^{(0)} \frac{\partial \bar{V}_z^{(1)}}{\partial X} + U_z^{(0)} \frac{\partial \bar{V}_z^{(1)}}{\partial Z} \right) \mathbf{e}_z \\ + \frac{10}{3} \pi R_c^{-1/2} \text{Re} \left[ \exp(i\varphi_p) \left\{ \begin{array}{l} -\zeta \left[ \frac{\partial \delta(\mathbf{R})}{\partial Z} \mathbf{e}_x + \frac{\partial \delta(\mathbf{R})}{\partial X} \mathbf{e}_z \right] \\ + 2\alpha_z \left[ \frac{\partial \delta(\mathbf{R})}{\partial X} \mathbf{e}_x - \frac{\partial \delta(\mathbf{R})}{\partial Z} \mathbf{e}_z \right] \end{array} \right\} \right], \end{aligned} \quad (4.18a)$$

$$\nabla \cdot U^{(1)} = 0. \quad (4.18b)$$

Similar to our strategy in (2.4), we transfer the boundary condition (4.15c) to the average locations of the walls instead of enforcing  $U^{(1)} = \mathbf{0}$  at the wavy walls, such that  $U^{(1)} = \mathbf{0}$  is enforced at the wavy wall to the first order (Van Dyke 1975)

$$U^{(1)} = \pm \frac{1}{2} \frac{\partial U^{(0)}}{\partial Z} R_c^{1/2} \text{Re}\{\exp[i(\varphi_p + \kappa X)]\}, \quad \text{at } \mathbf{R} = (X, Y, Z_{\pm}) \quad (4.19a)$$

$$U^{(1)} = \mathbf{0}, \quad X \rightarrow \infty, \quad (4.19b)$$

where  $Z_{\pm} = \{Z_-, Z_+\}$  denotes the  $Z$ -coordinates of the average locations of the walls.

4.3. Matching inner and outer solutions

Matching the inner and outer solutions enables us to calculate the lift force on the particle in the  $z$ -direction. From (4.1a,b) and (4.14a,b), we know that the perturbation velocity component at the origin  $u_z(\mathbf{R} = \mathbf{0})$ , i.e. the lateral migration velocity of the particle relative to the undisturbed flow, can be determined from the difference between  $\epsilon^3 U_z(\mathbf{R} = \mathbf{0})$  and  $\epsilon u_{1,z}(\mathbf{R} = \mathbf{0})$ . The migration velocity  $u_z(\mathbf{R} = \mathbf{0})$  gives rise to an inertial lift force acting on the particle in the  $z$  direction (Schonberg & Hinch 1989; Hogg 1994; Asmolov 1999) (see derivations of the force balance in Appendix C). Given the characteristic force scale  $\mu a U'_m$ , the dimensionless lift force on the particle  $F_{L,z}$  is then

$$F_{L,z} = 6\pi u_z = 6\pi\epsilon^3 \lim_{R \rightarrow 0} (U_z - \epsilon^{-2} u_{1,z}). \tag{4.20}$$

Since  $u_{1,z}(\mathbf{R})$  has already been obtained in (4.13), we now provide a strategy to numerically solve  $U_z$ . We first convert the partial differential equations (PDEs) (4.17) and (4.18) with Fourier transforms, obtaining governing equations for  $\tilde{U}^{(0)}(k_x, k_y, Z)$  and  $\tilde{U}^{(1)}(k_x, k_y, Z)$ , where the tildes denote quantities in the frequency domain, and  $k_x$  and  $k_y$  are frequencies. We further convert these PDEs into ordinary differential equations (ODEs) for  $\tilde{U}_z^{(0)}$  and  $\tilde{U}_z^{(1)}$ , respectively. Numerically solving the ODEs for  $\tilde{U}_z^{(0)}$  and  $\tilde{U}_z^{(1)}$  and performing inverse Fourier transforms will enable us to obtain  $F_{L,z}$  at different orders of  $\epsilon_w$  based on (4.20). The detailed derivations for the ODEs are documented in Appendix D.1.

After solving  $\tilde{U}_z^{(1a)}$  and  $\tilde{U}_z^{(1b)}$  for arbitrary values of  $k_x$  and  $k_y$ , we further evaluate the normalized lift force by performing the following inverse Fourier transform:

$$F_{L,z} = F_{L,z}^{(0)} + \epsilon_w F_{L,z}^{(1)} + O(\epsilon_w^2), \tag{4.21a}$$

$$F_{L,z}^{(0)} = 6\pi\epsilon^3 \operatorname{Re} \left[ \int_{-\infty}^{+\infty} \int_{-\infty}^{+\infty} \tilde{U}_z^{(0)}(k_x, k_y, 0) dk_x dk_y \right], \tag{4.21b}$$

$$F_{L,z}^{(1)} = 6\pi\epsilon^3 \operatorname{Re} \left[ \int_{-\infty}^{+\infty} \int_{-\infty}^{+\infty} \tilde{U}_z^{(1)}(k_x, k_y, 0) dk_x dk_y \right]. \tag{4.21c}$$

According to (D6)–(D7),  $\tilde{U}_z^{(1)}$  can be written in a form with the underlying parameters  $\mathcal{X}_p$  and  $\mathcal{Z}_p$  separated

$$\tilde{U}_z^{(1)}(k_x, k_y, 0) = \frac{1}{2} [\exp(i\varphi_p) \tilde{U}_z^{(1a)}(\check{k}_x, k_y, 0) + \exp(-i\varphi_p) \tilde{U}_z^{(1b)}(\hat{k}_x, k_y, 0)], \tag{4.22}$$

where  $\check{k}_x = k_x - \kappa$ ,  $\hat{k}_x = k_x + \kappa$  and the particle’s coordinate components  $\mathcal{X}_p$  and  $\mathcal{Z}_p$  are embedded in  $\varphi_p$  and  $\tilde{U}_z^{(1a/b)}$ , respectively. Compared with (4.20), (4.21) does not contain any terms from  $u_{1,z}(\mathbf{R} = \mathbf{0})$  (4.13), because the two-dimensional Fourier transform of a strainlet velocity field is imaginary at the origin (Schonberg & Hinch 1989; Hogg 1994; Asmolov 1999). Thus,  $F_{L,z}$  is different from the outer solution  $U_z(\mathbf{R} = \mathbf{0})$  only by a factor of  $6\pi\epsilon^3$ . Notably,  $F_{L,z}$  is a function of  $\mathcal{X}_p$ ,  $\mathcal{Z}_p$ ,  $\omega$ ,  $\epsilon$  and  $\epsilon_w$ .

It is important to note that the ODEs for  $\tilde{U}_z^{(1a)}$  and  $\tilde{U}_z^{(1b)}$  (D8)–(D12) reduce to the same form in the limit of  $\omega \rightarrow 0$ , giving rise to  $\tilde{U}_z^{(1a)}(\check{k}_x, k_y, 0) = \tilde{U}_z^{(1b)}(\hat{k}_x, k_y, 0)$ . In this case, one can show that  $F_{L,z}^{(1)}$  is in phase with the sinusoidal profile of the wavy channel (4.22).

We compute  $F_{L,z}^{(0)}$ ,  $F_{L,z}^{(1)}$  and  $F_{L,z}$  across the channel based on (4.21) and present the results in figures 6–8, respectively. Figure 6 shows  $\epsilon^{-3} R_c^{1/2} F_{L,z}^{(0)}$  as a function of  $\mathcal{Z}_p$  at varying  $R_c$ .



Particle focusing in a wavy channel

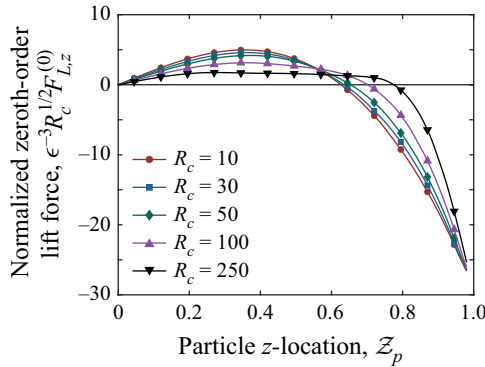


Figure 6. Normalized zeroth-order lift force  $\epsilon^{-3}R_c^{1/2}F_{L,z}^{(0)}$  as a function of the  $\mathcal{Z}$ -coordinate of the particle  $\mathcal{Z}_p$  at varying channel Reynolds numbers  $R_c$ . For varying particle  $z$ -location  $\mathcal{Z}_p$ , the outer solution  $U_z^{(0)}(R = 0)$  is different from  $F_{L,z}^{(0)}$  only by a factor of  $6\pi\epsilon^3$  (4.21b).

The zeroth-order lift-force component  $F_{L,z}^{(0)}$  points towards the wall, or outwards, when the particle is in the inner part of the channel;  $F_{L,z}^{(0)}$  points towards the centreline, or inwards, when the particle gets close to the wall. As  $R_c$  increases, the equilibrium position of  $F_{L,z}^{(0)}$  shifts outwards, and the magnitude of  $\epsilon^{-3}R_c^{1/2}F_{L,z}^{(0)}$  decreases in the inner part of the channel. Our computed zeroth-order lift force is consistent with the lift force reported in Asmolov (1999).

The first-order lift force  $F_{L,z}^{(1)}$  varies in both the  $x$ - and  $z$ -directions and is a function of the channel Reynolds number  $R_c$  and the frequency  $\omega$ . Figures 7(a) and 7(b) show the variation of the normalized first-order lift force  $\epsilon^{-3}R_c^{1/2}F_{L,z}^{(1)}$  in a period of the channel for two pairs of  $R_c$  and  $\omega$ ; due to the sharp variations close to the walls, we adopt a moderate range of  $[-200, 200]$  for  $\epsilon^{-3}R_c^{1/2}F_{L,z}^{(1)}$  to better illustrate the variations in the bulk of the channel. The lift force  $F_{L,z}^{(1)}$  has a relatively low magnitude close to the centre of the channel, and its magnitude increases sharply close to the walls. The sign of  $F_{L,z}^{(1)}$  also varies with the phase angle of the particle in the  $x$ -direction  $\varphi_p$ , where  $\varphi_p = \omega\mathcal{X}_p$ . According to (4.21c), for any particle location,

$$F_{L,z}^{(1)}(\mathcal{X}_p, \mathcal{Z}_p) = \sin(\varphi_p)F_{L,z}^{(1)}(\mathcal{X}_p = 0, \mathcal{Z}_p) + \cos(\varphi_p)F_{L,z}^{(1)}\left(\mathcal{X}_p = \frac{\pi}{2\omega}, \mathcal{Z}_p\right). \quad (4.23)$$

Thus, we present  $F_{L,z}^{(1)}$  as a function of  $\mathcal{Z}_p$  at two phase angles in the  $x$ -direction, i.e.  $\varphi_p = 0$  and  $\varphi_p = \pi/2$  in figures 7(c) and 7(d), respectively. Figure 7(c) shows the influence of  $R_c$  at  $\omega = 2$ , and figure 7(d) shows the influence of  $\omega$  at  $R_c = 100$ . Notably, increasing  $R_c$  and decreasing  $\omega$  have a similar effect on the  $\mathcal{Z}_p$ - $F_{L,z}^{(1)}$  relationship, as illustrated in the resemblance in the variation of the curves between figures 7(c) and 7(d). Figure 7(d) also shows a vanishing  $F_{L,z}^{(1)}$  for  $\varphi_p = \pi/2$  in the limit of  $\omega \rightarrow 0$ , which accords with our observation that  $F_{L,z}^{(1)}$  is in phase with the wavy channel.

By adding  $F_{L,z}^{(0)}$  and  $F_{L,z}^{(1)}$ , we show the variation of  $\epsilon^{-3}F_{L,z}$  across the channel for two pairs of  $R_c$  and  $\omega$  in figures 8(a) and 8(b). We are interested in the locations where  $F_{L,z} = 0$ , i.e. the zero contour lines. Particles are unstable on the zero contour line at

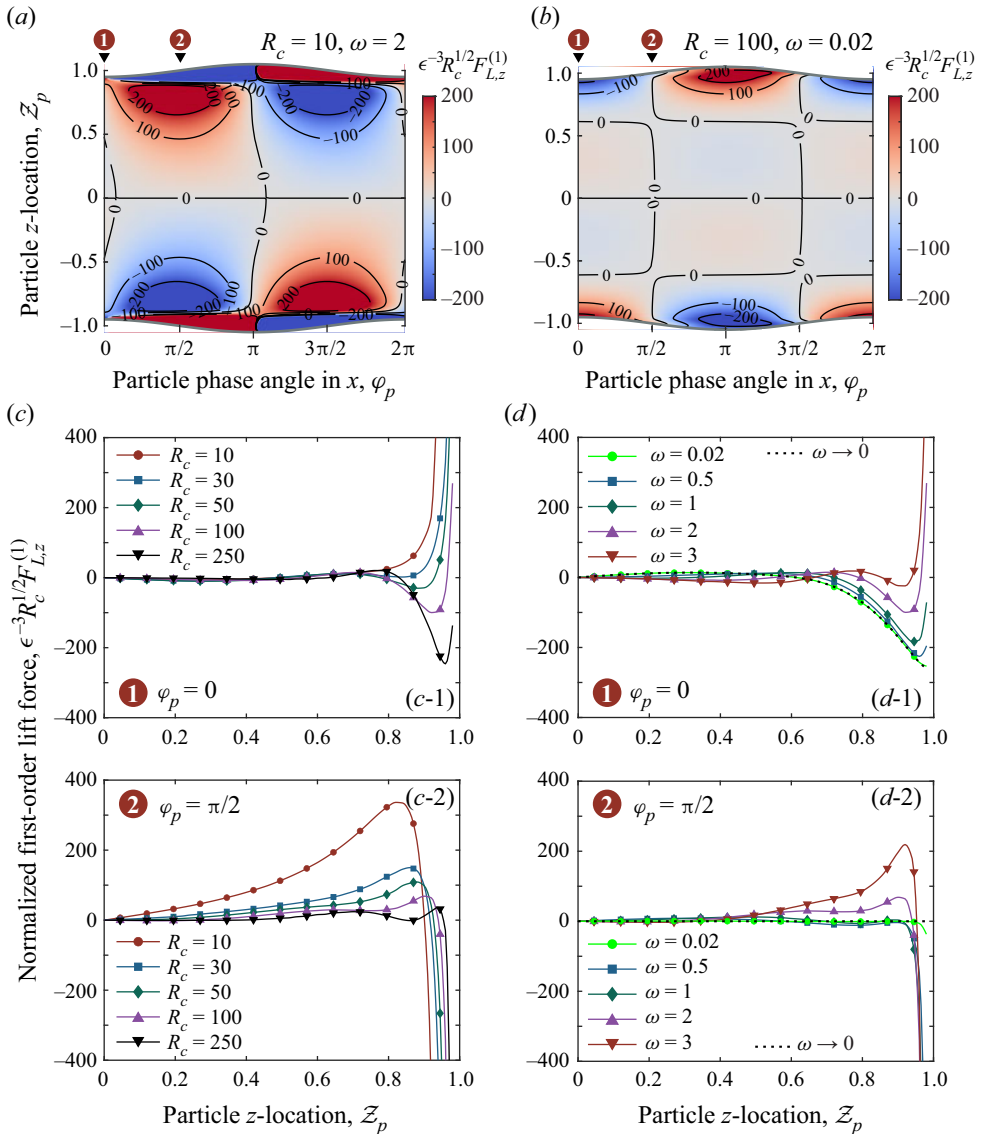


Figure 7. Normalized first-order (in  $\epsilon_w$ ) lift force. (a,b) Value of  $\epsilon^{-3}R_c^{1/2}F_{L,z}^{(1)}$  as a function of the  $\mathcal{Z}$ -coordinate of the particle  $\mathcal{Z}_p$  and the particle's phase angle in the  $x$ -direction  $\varphi_p$  for (a)  $R_c = 10, \omega = 2$  and (b)  $R_c = 100, \omega = 0.02$ . Results for  $|\mathcal{Z}_p| > 1$  are obtained by extrapolation. (c) Value of  $\epsilon^{-3}R_c^{1/2}F_{L,z}^{(1)}(\varphi_p = 0)$  and  $\epsilon^{-3}R_c^{1/2}F_{L,z}^{(1)}(\varphi_p = \pi/2)$  as a function of  $\mathcal{Z}_p$  at varying  $R_c$  and  $\omega = 2$ . Here, a scaling factor  $R_c^{1/2}$  makes the order of magnitude consistent for varying  $R_c$ . (d) Value of  $\epsilon^{-3}R_c^{1/2}F_{L,z}^{(1)}(\varphi_p = 0)$  and  $\epsilon^{-3}R_c^{1/2}F_{L,z}^{(1)}(\varphi_p = \pi/2)$  as a function of  $\mathcal{Z}_p$  at varying  $\omega$  and  $R_c = 100$ . Dashed lines in (d) represent numerical solutions for  $\omega \rightarrow 0$ . For varying particle  $z$ -location  $\mathcal{Z}_p$ , the outer solution  $U_z^{(1)}(\mathbf{R} = \mathbf{0})$  is different from  $F_{L,z}^{(1)}$  only by a factor of  $6\pi\epsilon^3$  (D6a) and (4.21c).

Particle focusing in a wavy channel

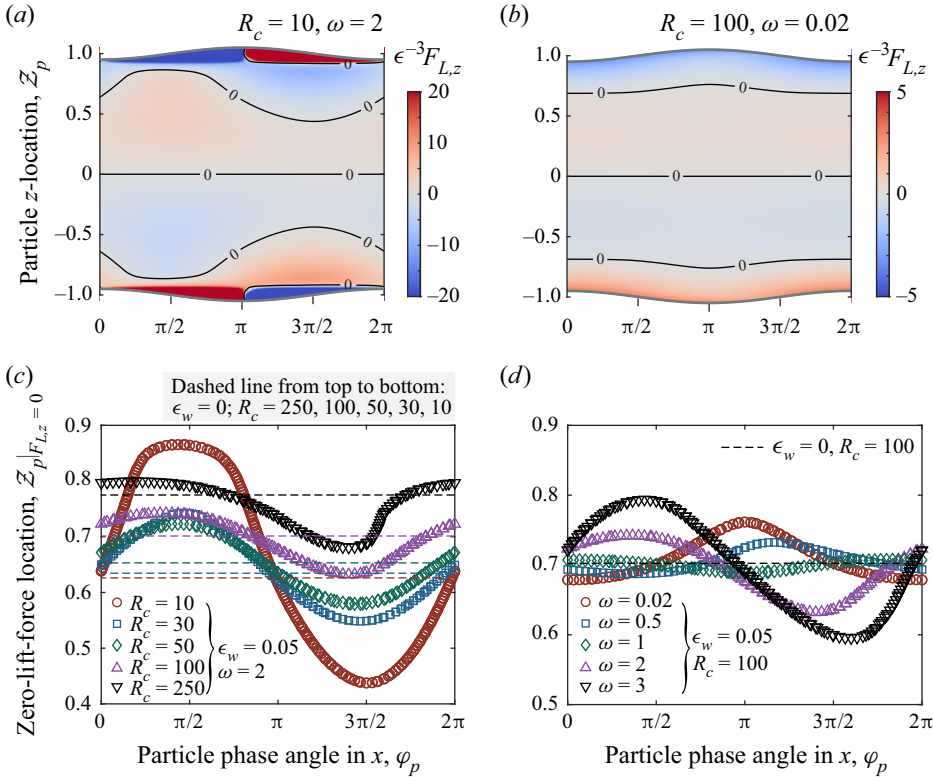


Figure 8. Normalized lift force  $\epsilon^{-3}F_{L,z}$  as a function of the  $Z$ -coordinate of the particle  $Z_p$  and the phase angle of the particle in the  $x$ -direction  $\varphi_p$  for (a)  $R_c = 10, \omega = 2$  and (b)  $R_c = 100, \omega = 0.02$ . (c) Zero-lift-force location  $Z_p|_{F_{L,z}=0}$  as a function of  $\varphi_p$  for varying  $R_c$  and  $\omega = 2$ . (d) Zero-lift-force location  $Z_p|_{F_{L,z}=0}$  as a function of  $\varphi_p$  for varying  $\omega$  and  $R_c = 100$ .  $\epsilon_w = 0.05$  for all panels.

the centre because the nearby lift force points away from the centreline. In figure 8(a), we also observe a pair of unstable zero contour lines along part of the channel close to the walls (mostly within  $\varphi_p \in [\pi, 2\pi]$ ). These near-wall zero contour lines arise because  $F_{L,z}^{(0)}$  and  $F_{L,z}^{(1)}$  have different signs in these regions and  $F_{L,z}^{(1)}$  has a large magnitude close to the walls for  $R_c = 10, \omega = 2$  (figure 7c). Since previous studies report that the lift force directs particles away from the walls (Asmolov 1999; Di Carlo *et al.* 2009), it is unlikely that particles may be pushed toward the walls as they approach these unstable contour lines. Note that we compute the undisturbed flow and the perturbation velocity up to the first order in  $\epsilon_w$ . Due to the sharp variations in the first-order flow and perturbation fields near the walls, higher-order computations may be necessary for a better understanding of the near-wall lift force, which is, however, beyond the scope of our current analyses. The critical stable zero contour lines are close to  $Z_p = \pm 0.6$ . The shapes of these stable zero contour lines do not always follow the configuration of the channel. For a large  $R_c$  and a small  $\omega$  (figure 8b), the shape of the stable zero contour line is in phase with the configuration of the wavy channel. As  $R_c$  decreases or  $\omega$  increases, the shape of the stable zero contour line gradually becomes out of phase, as shown in figures 8(c) and 8(d).

Finally, it is important to note that the zero-lift-force locations are generally different from the focusing locations of particles in wavy channels. Unlike the situation in straight channels where both types of locations coincide, the secondary flow in wavy channels

makes particles move in the  $z$ -direction constantly. Thus, even if a particle finally stabilizes in a wavy channel, it never truly reaches equilibrium. To resolve the focusing location, it is necessary to analyse the particle trajectory, which we address in § 5.

### 5. Particle focusing locations

After obtaining the lift force on the particle, we here provide a strategy to predict the focusing locations of the particle in the wavy channel. For this, we come back to the laboratory frame (figure 3). We use  $\mathcal{R}'_p(t) = (\mathcal{X}'_p(t), \mathcal{Z}'_p(t))$  to denote the instantaneous location of the particle centre. Instead of solving the fluid stress over the surface of the particle and using Newton's second law, we employ the modified Maxey–Riley equation to analyse the trajectory of the particle (Maxey & Riley 1983; Ferry & Balachandar 2001)

$$m_p \frac{dU'_p}{dt'} = 6\pi a \mu (\bar{\mathbf{V}}' - U'_p) + m_f \frac{D\bar{\mathbf{V}}'}{Dt'} + \frac{1}{2} m_f \left( \frac{D\bar{\mathbf{V}}'}{Dt'} - \frac{dU'_p}{dt'} \right) + (m_p - m_f) \mathbf{g}' + \frac{6\pi a^2 \mu}{\sqrt{v}} \frac{d^{1/2}}{dt'^{1/2}} (\bar{\mathbf{V}}' - U'_p) + F'_L, \tag{5.1}$$

where  $m_p$  is the particle mass,  $m_f$  is the fluid mass displaced by the particle,  $\bar{\mathbf{V}}' = \bar{\mathbf{V}}'(\bar{\mathcal{R}}'_p(t))$  is the particle-free fluid velocity at the instantaneous particle centre,  $D/Dt'$  is the material derivative following a fluid parcel,  $\mathbf{g}'$  is the gravitational acceleration and  $\mu$  is the dynamic viscosity of the fluid. Additionally,  $dU'_p/dt' = \mathbf{a}'_p$  is the particle acceleration defined in § 3. The terms on the right-hand side of (5.1) represent the Stokes drag, fluid acceleration, added mass, gravity, Basset force and lift force on the particle. For the scaling analysis, we choose  $l$  as the characteristic length,  $U'_m$  as the characteristic velocity,  $l/U'_m$  as the characteristic time and  $\mu a U'_m$  as the characteristic lift force. By comparing the forcing terms, we neglect the Basset force and write (5.1) in the following dimensionless form:

$$\left( 1 + \frac{1}{2} \frac{\rho_f}{\rho_p} \right) Stk \frac{D(U_p - \bar{\mathbf{V}})}{Dt} = - (U_p - \bar{\mathbf{V}}) + \left( \frac{\rho_f}{\rho_p} - 1 \right) Stk \frac{D\bar{\mathbf{V}}}{Dt} + B \mathbf{e}_g + \frac{1}{6\pi} F_L, \tag{5.2}$$

where  $\rho_p$  is the particle density,  $B = 2a^2(\rho_p - \rho_f)\mathbf{g}'/(9\mu U'_m)$  is the buoyancy number,  $\mathbf{e}_g$  is a unit vector in the direction of the gravitational force and  $Stk$  is the Stokes number. Specifically,  $Stk$  is the ratio between the particle relaxation time  $t_p$  and the characteristic time of the flow  $t_f$ , where  $t_p = 2\rho_p a^2/(9\mu)$  and  $t_f = l/U'_m$ . Since our asymptotic parameter  $\epsilon = R_c^{1/2} a/l = (\rho_f U'_m l/\mu)^{1/2} a/l$ , we have

$$Stk = \frac{2}{9} \frac{\rho_p}{\rho_f} \epsilon^2 \ll 1. \tag{5.3}$$

For a neutrally buoyant particle, (5.2) can be converted into a differential equation of the particle location

$$\frac{1}{3} \epsilon^2 \ddot{\mathcal{R}}_p + \dot{\mathcal{R}}_p = \bar{\mathbf{V}} + \frac{1}{3} \epsilon^2 \frac{D\bar{\mathbf{V}}}{Dt} + \frac{1}{6\pi} F_L, \tag{5.4}$$

where  $\dot{\mathcal{R}}_p$  and  $\ddot{\mathcal{R}}_p$  denote the velocity and acceleration of the particle, respectively. Here,  $\dot{\mathcal{R}}_p = U_p$ . With  $\bar{\mathbf{V}}$  and  $F_L$  solved in previous sections, we can simulate the trajectory of

the particle based on (5.4). By holding  $R_c$ ,  $\omega$ , and  $\epsilon_w$  constant, we find that the simulated trajectory gradually stabilizes over time for any initial particle location. We regard the stabilized trajectory in a period of the channel as particle focusing locations. Additionally, the stabilized trajectory asymptotes to a constant shape as  $\epsilon$  decreases; as indicated by the stabilized range of the particle's  $z$ -location (inset of figure 9b), the stabilized trajectory for  $\epsilon = 0.2$  is not significantly different from that for  $\epsilon = 0.1$ .

In figure 9(a), we show two sets of simulated particle trajectories in channels with amplitudes  $\epsilon_w = 0, 0.05$  and  $0.1$  for  $R_c = 10, \omega = 2$  and  $\epsilon = 0.2$ . The results in figure 9(a-1) are based on both the zeroth-order and first-order lift forces, i.e.  $F_{L,z}$ . For all three values of  $\epsilon_w$ , the particle is initially at  $Z_p = 0.1$  and gradually migrates towards the stable focusing locations. When  $X_p = 2000$ , the movement of the particle is stabilized: for the straight channel ( $\epsilon_w = 0$ ),  $Z_p$  does not change over time and agrees with the asymptotic solution based on Asmolov (1999); for the wavy channels ( $\epsilon_w = 0.05$  and  $0.1$ ),  $Z_p$  oscillates sinusoidally about an average level. As  $\epsilon_w$  increases, the amplitude of  $Z_p$  also increases but is always lower than  $\epsilon_w$ ; additionally, the average focusing location shifts slightly inwards. Interestingly, the channel length for particle focusing is independent of  $\epsilon_w$ , but is significantly impacted by  $\epsilon$  (figure 9b). We notice that when  $\epsilon$  becomes very small, e.g.  $\epsilon = 0.01$ , a significantly longer channel is required to achieve particle focusing. Because  $F_L \sim O(\epsilon^3)$ , a smaller  $\epsilon$  gives rise to a smaller lift force, which causes the particle to migrate more slowly.

To understand which part of the lift force contributes to the oscillation and shifting of the focusing locations, we only keep the zeroth-order lift force  $F_{L,z}^{(0)}$  and repeat the simulations for the particle trajectories. By comparing the insets of figures 9(a-1) and 9(a-2), we find only slight differences in the average focusing locations for  $\epsilon_w = 0.05$  and  $0.1$ . All other features of figures 9(a-1) and 9(a-2) are indistinguishable. The zeroth-order lift force is thus the governing force for particle focusing in wavy channels. Despite its sinusoidal characteristics, the first-order lift force  $F_{L,z}^{(1)}$  plays an almost negligible role in the oscillation of the particle in the steady state. Rather, the oscillation of the particle stems from the interaction between  $F_{L,z}^{(0)}$  and the periodic flow  $\bar{\mathbf{V}}$ . Furthermore, due to its sinusoidal characteristics,  $F_{L,z}^{(1)}$  does not induce any variation in the length of the channel for focusing in figure 9(a).  $F_{L,z}^{(1)}$  mainly contributes to the slight variation in the average focusing location in the  $z$ -direction  $\bar{Z}_p$ .

We now mathematically understand the role of  $F_{L,z}^{(1)}$  in influencing  $\bar{Z}_p$  in the asymptotic limit  $\epsilon_w \ll 1$  and  $\epsilon \ll 1$ . Further neglecting the  $O(\epsilon^2)$  terms in (5.4), we obtain the following equation for a neutrally buoyant particle:

$$-V_s = \frac{1}{6\pi} F_L, \tag{5.5}$$

where  $V_s = \bar{\mathbf{V}} - \dot{\mathcal{R}}_p = \bar{\mathbf{V}} - U_p$  is the slip velocity defined in § 3, and  $-V_{s,z}$  corresponds to the lateral migration velocity of the particle relative to the particle-free flow  $U_{lateral}$ . Denoting the average slip velocity in the  $z$ -direction over time as  $\overline{V_{s,z}}$ , then  $\overline{V_{s,z}(Z_p(t))} = 0$  represents the stable state. We have the stability condition

$$\overline{F_{L,z}(Z_p(t))} = 0. \tag{5.6}$$

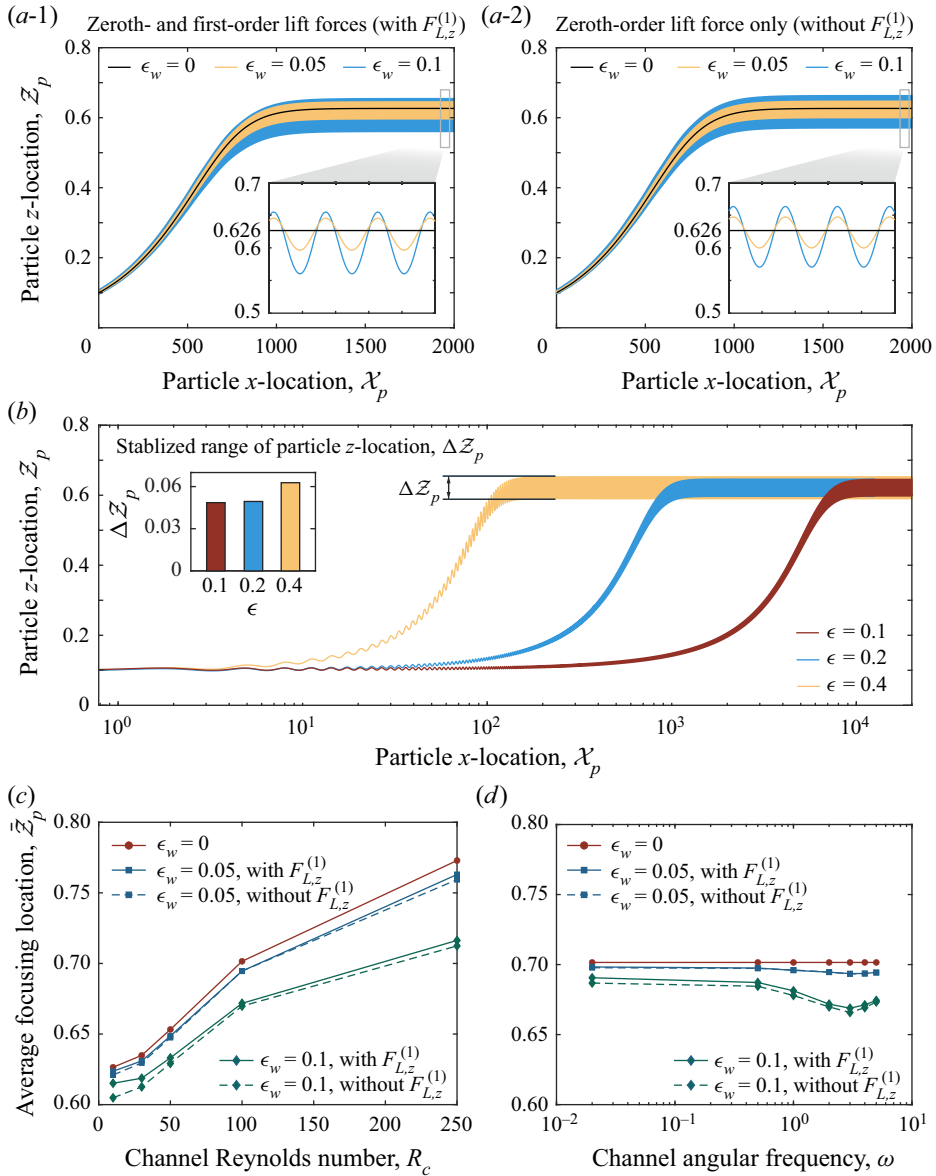


Figure 9. (a) Simulated trajectories of a particle initially located at  $\bar{Z}_p = 0.1$  in channels with varying amplitude  $\epsilon_w$ , where the lift forces are the zeroth- and first-order lift forces (a-1) and zeroth-order lift force only (a-2). Here,  $R_c = 10$ ,  $\omega = 2$  and  $\epsilon = 0.2$ . (b) Influence of asymptotic parameter  $\epsilon$  on the simulated trajectory of a particle initially located at  $\bar{Z}_p = 0.1$ , where  $R_c = 10$ ,  $\omega = 2$ ,  $\epsilon_w = 0.05$  and the lift force contains both the zeroth- and first-order lift forces. (c) Average focusing location  $\bar{Z}_p$  as a function of channel Reynolds number  $R_c$  for varying  $\epsilon_w$ , where  $\omega = 2$ . (d) Average focusing location  $\bar{Z}_p$  as a function of channel angular frequency  $\omega$  for varying  $\epsilon_w$ , where  $R_c = 100$ .

Because  $\epsilon_w$  is small, the particle does not deviate significantly from  $\bar{Z}_p$ . Thus, we can expand  $F_{L,z}(Z_p(t))$  into a Taylor series about  $\bar{Z}_p$

$$F_{L,z}(Z_p) = F_{L,z}(\bar{Z}_p) + (Z_p - \bar{Z}_p) \left. \frac{dF_{L,z}}{dZ_p} \right|_{Z_p=\bar{Z}_p} + O((Z_p - \bar{Z}_p)^2). \quad (5.7)$$

Neglecting high-order terms, the stability condition (5.6) becomes

$$\overline{F_{L,z}(\bar{Z}_p)} + (\bar{Z}_p - \bar{Z}_p) \left. \frac{dF_{L,z}}{dZ_p} \right|_{Z_p=\bar{Z}_p} = 0, \tag{5.8}$$

where  $\bar{Z}_p - \bar{Z}_p = \int (\bar{V}_z/\bar{V}_x) d\mathcal{X}_p$ . Evaluating (5.8) with results from (2.5) and (4.21) and only keeping the leading-order terms in  $\epsilon_w$ , we finally arrive at the following implicit expression for  $\bar{Z}_p$ :

$$\begin{aligned} F_{L,z}^{(0)}(\bar{Z}_p) - \frac{\epsilon_w}{\omega(1 - \bar{Z}_p^2)} \left\{ \text{Re}[\hat{\mathcal{V}}_z(\bar{Z}_p)] \left. \frac{dF_{L,z}^{(0)}}{dZ_p} \right|_{Z_p=\bar{Z}_p} \right. \\ + \frac{\epsilon_w^2}{2\omega(1 - \bar{Z}_p^2)} \left\{ \text{Re}[\hat{\mathcal{V}}_z(\bar{Z}_p)] \left. \frac{\partial F_{L,z}^{(1)}}{\partial Z_p} \right|_{Z_p=\bar{Z}_p, \varphi_p=\pi/2} \right. \\ \left. \left. + \text{Im}[\hat{\mathcal{V}}_z(\bar{Z}_p)] \left. \frac{\partial F_{L,z}^{(1)}}{\partial Z_p} \right|_{Z_p=\bar{Z}_p, \varphi_p=0} \right\} \right\} = 0. \end{aligned} \tag{5.9}$$

Clearly, the terms related to  $F_{L,z}^{(1)}$  are of  $O(\epsilon_w^2)$ , which explains the limited contribution of  $F_{L,z}^{(1)}$  to  $\bar{Z}_p$ . To interpret this result physically, the interaction between the first-order lift force and the first-order particle-free flow is not comparable to the interaction between the zeroth-order lift force and the first-order particle-free flow.

By repeating the simulations of particle trajectories with (5.4), we investigate the influence of channel Reynolds number  $R_c$  and channel angular frequency  $\omega$  on the average focusing location  $\bar{Z}_p$ . Figure 9(c) shows  $\bar{Z}_p$  vs  $R_c$  for  $\epsilon_w = 0, 0.05$  and  $0.1$ , where  $\omega = 2$ . As  $R_c$  increases,  $\bar{Z}_p$  shifts outwards for all three values of  $\epsilon_w$ . For a constant  $R_c$ ,  $\bar{Z}_p$  gets closer to the centre of the channel as  $\epsilon_w$  increases. In figure 9(d), we show the relationship between  $\bar{Z}_p$  and  $\omega$  for  $\omega \in [0.02, 5]$  and  $R_c = 100$ .  $\bar{Z}_p$  does not vary monotonically with  $\omega$ . When  $\omega$  approaches zero, particles behave as if in a straight channel; thus,  $\bar{Z}_p$  of varying  $\epsilon_w$  also approaches  $\bar{Z}_p$  in the straight channel. For  $\omega > 2$ ,  $\bar{Z}_p$  slightly increases with  $\omega$ . However, the influence of  $\epsilon_w$  on  $\bar{Z}_p$  is much less obvious than that of  $R_c$ . These results suggest that adjusting  $\omega$  is not an effective strategy for altering the particle focusing locations.

## 6. Experiments

In this section, we experimentally investigate particle focusing in wavy channels and compare the results with those obtained from a straight channel. All channels have the same width  $l$ , where  $l = 2h = 1.18$  mm. The experimental set-up and procedures are described in Appendix E. Briefly, we use two sizes of particles with average radii  $a = 200$   $\mu\text{m}$  and  $60$   $\mu\text{m}$ , which correspond to  $a/h = 0.17$  and  $0.05$ , respectively. The particles are neutrally buoyant in our water–glycerol solution. We inject the particle suspensions in the channels and observe particle behaviours at a fixed location. The distance from the channel inlet and the observation location is denoted as  $L$ , where  $L = 550$  mm (figure 10a). It is important to note that our theoretical analyses are based on ideal assumptions  $\epsilon = R_c^{1/2} a/l \ll 1$ ,  $a/h \ll 1$ ,  $\epsilon_w \ll 1$ , and infinite channel depth  $w$ .

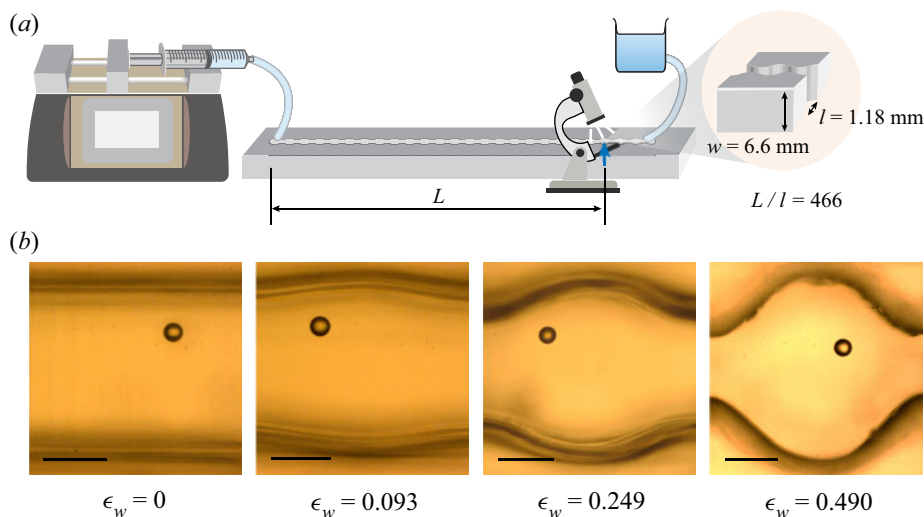


Figure 10. (a) Schematics of the experimental set-up, where  $L$  denotes the distance between the channel inlet and the fixed observation location. (b) Images of a polystyrene particle in channels with varying amplitudes. All four channels have average width  $l = 1.18$  mm. The scale bars denote  $500 \mu\text{m}$ .

Since these parameters are finite in practice, in addition to testing our asymptotic theory, we aim to experimentally characterize particle focusing when the real set-up deviates from our ideal assumptions.

In figure 11, we present particle distributions at  $L/l = 466$  in channels with varying amplitude  $\epsilon_w$  at varying  $R_c$ , where  $a/h = 0.17$ . For a constant  $\epsilon_w$ , particles gradually get focused as  $R_c$  increases. As predicted by our asymptotic theory, we observe that particles are focused on two symmetric lines, which is a hallmark of a strong inertial lift effect. At a small  $\epsilon_w$ , e.g.  $\epsilon_w = 0.093$ , the focusing locations are along two curves that are almost parallel to the channel profiles. For a relatively large  $\epsilon_w$ , e.g.  $\epsilon_w = 0.249$  or  $0.490$ , the focusing curves deviate from the channel profiles and flatten out as  $R_c$  increases. When  $\epsilon_w = 0.490$  and  $R_c = 250$ , some particles even get trapped in the expanded sections of the channels. To understand these variations, we compute the streamlines in the wavy channels with Ansys Fluent. For all values of  $\epsilon_w$  and  $R_c$ , the focusing curves overlap two symmetric streamlines (figure 11), indicating that the particle trajectories follow the particle-free streamlines. For a small  $\epsilon_w$  or  $R_c$ , all streamlines mostly follow the shape of the channels; however, when both  $\epsilon_w$  and  $R_c$  are large enough, vortices appear in the expanded section, and the continuous streamlines only appear in the middle part of the channel. Consequently, most particles are focused along the flattened streamlines close to the centre, but some particles are occasionally trapped in the vortices. Furthermore, to probe the capability of our asymptotic theory in predicting particle focusing locations, we present in figure 11 the simulated results based on the asymptotic lift force  $F_{L,z}^{(0)}$  and (5.4). Remarkably, although the assumptions  $\epsilon \ll 1$  and  $a/h \ll 1$  are not strictly satisfied in the experiments, the asymptotic theory provides fairly close estimates of the experimental focusing locations.

Another takeaway from figure 11 is that wavy channels can help particles focus at a slightly lower Reynolds number  $R_c$  than the straight channel while keeping the average channel width  $l$  and observation position  $L/l$  constant. For  $R_c = 10$ , for instance, particles are almost fully focused in the wavy channels, whereas little focusing is observed in the straight channel. To rationalize these observations, we present in figure 12(a) the



Particle focusing in a wavy channel

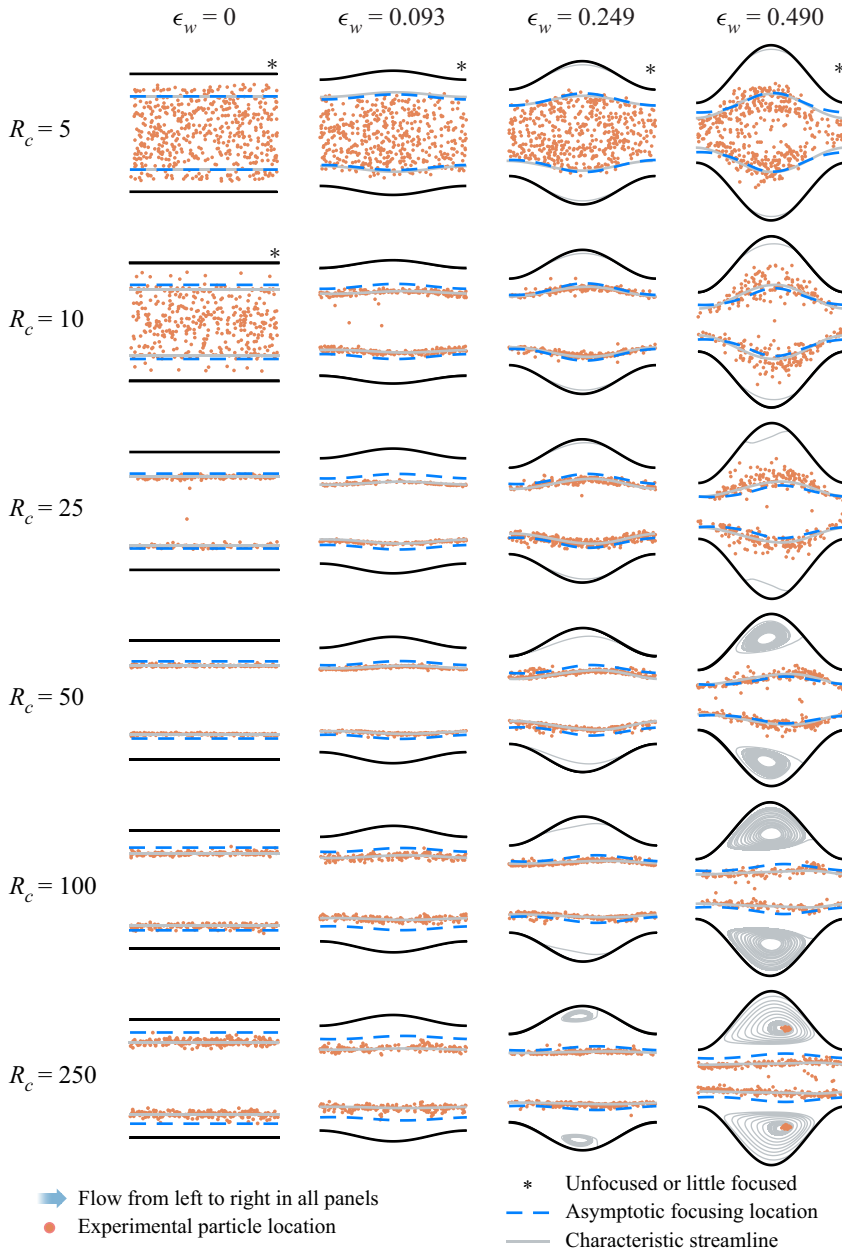


Figure 11. Experimental and asymptotic particle focusing locations in channels with different amplitudes  $\epsilon_w$  at varying channel Reynolds numbers  $R_c$ . Asymptotic focusing locations are based on simulations in § 5, and experimental focusing locations are measured at  $L/l = 466$ . (\*) Asterisks denote little or no focusing at a low  $R_c$ . Here,  $a/h = 0.17$ .

distributions of two sizes of particles at increasing  $R_c$  in the straight channel and the wavy channel with  $\epsilon_w = 0.093$ . The critical  $R_c$  for the focusing transition is of  $O(10)$  for  $a/h = 0.17$ , and the critical  $R_c$  is of  $O(10^2-10^3)$  for  $a/h = 0.05$ . The variation in the critical  $R_c$  with  $a/h$  can be explained by the asymptotic results: in figures 6 and 7, we show that  $F_{L,z} \sim O(\epsilon^3 R_c^{-1/2})$ . We can bring  $F_{L,z}$  back into the dimensional format

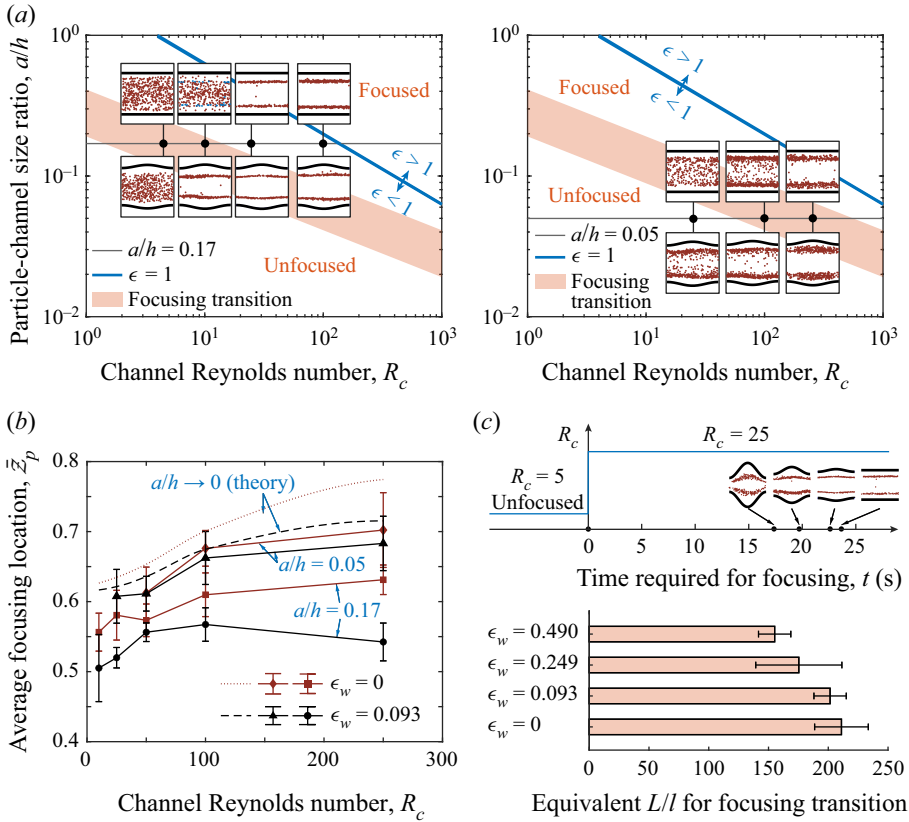


Figure 12. (a) Comparison of particle distributions in the wavy and straight channels at increasing channel Reynolds number  $R_c$ , where  $\epsilon_w = 0.093$  for the wavy channel, and the normalized particle sizes  $a/h$  are 0.17 (left) and 0.05 (right). (b) Experimentally obtained average focusing location  $\bar{z}_p$  as a function of  $R_c$  compared with results based on the asymptotic theory. (c) Transition of the focusing states occurring as the channel Reynolds number  $R_c$  increases from 5 to 25 at time  $t = 0$ . The upper panel shows the time required for the particles to be focused in channels with varying amplitudes  $\epsilon_w$ . This time is converted into the equivalent normalized channel lengths  $L/l$  in the lower panel. Here,  $a/h = 0.17$ . The online supplementary movie 1 available at <https://doi.org/10.1017/jfm.2023.558> shows particle focusing in a wavy channel occurring as the channel Reynolds number increases from 5 to 25 at time  $t = 0$ .

$F'_{L,z} = C\mu U'_m R_c a^4 / l^3$  with  $\epsilon = R_c^{1/2} a / l$  and  $F'_{L,z} = \mu a U'_m F_{L,z}$ , where  $C$  is a constant. Moreover, the lift force must be in balance with a drag force  $F'_D$  during lateral migration, where  $F'_D = 6\pi\mu a U'_{lateral}$ . Since  $F'_{L,z} = F'_D$ , we obtain  $L_{focus} / l = U'_m / U'_{lateral} = (3\pi / 4C) R_c^{-1} h^3 / a^3$ , where  $L_{focus}$  is the length of the channel required for particle focusing. For our fixed length  $L/l$ , the critical  $R_c$  for particle focusing thus follows a power law with  $a/h$

$$R_{c,critical} = \frac{3\pi}{4C} \frac{l}{L} \left(\frac{a}{h}\right)^{-3}, \tag{6.1}$$

which coincides with the theories for a straight channel (Matas *et al.* 2004). We select  $C = 0.1-1$  and show the critical  $R_c$  as a function of  $a/h$  in figure 12(a).

The insets of figure 12(a) show that particles are focused at a slightly lower  $R_c$  in the wavy channel, especially for  $a/h = 0.17$ ; for the same  $R_c$  and  $l$ , it requires a shorter distance for particles to be focused in a wavy channel. This finding, however,

does not contradict the results in figure 9(a) based on the asymptotic theory. First, the experimentally obtained  $R_{c,critical}$  is of the same order of magnitude in both types of channels. Second, the difference in  $L_{focus}$  is due to the deviation from the asymptotic assumption  $a/h \ll 1$  in our experiments. For a finite-sized particle, we can still decompose  $F_{L,z}$  into  $F_{L,z}^{(0)} + \epsilon_w F_{L,z}^{(1)}$ . However, unlike the asymptotic case in which  $F_{L,z}^{(1)}$  varies sinusoidally along the  $x$ -direction at a constant  $\bar{Z}_p$  (4.21c), the symmetry is broken for a finite  $a/h$ ;  $F_{L,z}^{(1)}$  of a finite-sized particle has a higher magnitude in the constricted sections of the wavy channel than in the expanded sections. This is because the distance to the wall is now finite relative to the particle size, and a stronger hydrodynamic interaction with the wall gives rise to greater repulsion effects in the constricted section, leading to slightly faster particle focusing in wavy channels. This effect becomes weaker as the particle size approaches the asymptotic limit, e.g.  $a/h = 0.05$  in figure 12(a). Third, when  $\epsilon_w$  is even larger, e.g.  $\epsilon_w = 0.249$  and  $0.490$  in figure 11, the flattening of the continuous streamlines also causes the particles to experience stronger repulsion effects in the constricted sections.

Figure 12(b) shows the relationship between the average focusing location  $\bar{Z}_p$  and  $R_c$  for the channels with  $\epsilon_w = 0$  and  $0.093$ . As predicted by the asymptotic theory, the measured  $\bar{Z}_p$  is positively related to  $R_c$  for  $a/h = 0.05$ . However, as the particle size increases, the measured  $\bar{Z}_p$  gradually deviates from the asymptotic predictions and moves towards the centre of the channel. This behaviour is consistent with previous experimental observations in circular pipes (Matas *et al.* 2004) and square cross-section channels (Di Carlo *et al.* 2009). Because the motion of a finite-size particle causes a significant disturbance to the particle-free flow, it is well understood that the lift force is subject to a different scaling law than  $O(\epsilon^3 R_c^{-1/2})$  and that the equilibrium positions move closer to the centreline (Di Carlo *et al.* 2009; Hood *et al.* 2015). Additionally, the measured  $\bar{Z}_p$  in the wavy channel is consistently lower than that measured in the straight channel, which agrees with the asymptotic predictions (figures 9(c) and 11). Our experiments show that  $\bar{Z}_p$  starts to decrease for  $R_c = 250$  and  $\epsilon_w = 0.093$ ; by contrast, our asymptotic theory demonstrates this phenomenon only at a higher  $\epsilon_w$  (figure 11). This is because a finite-sized particle moves closer to the channel centreline, and  $\bar{Z}_p$  decreases at  $R_c = 250$  even for a relatively small  $\epsilon_w$ .

Finally, because the difference in the critical  $R_c$  for the focusing transition can be subtle in figure 11, we here provide a second strategy to demonstrate that particles get focused faster in wavy channels than in straight channels under the same conditions. Figure 12(c) shows the response of the particle distribution at  $L/l = 466$  in channels with varying  $\epsilon_w$  as  $R_c$  increases from 5 to 25 at time  $t = 0$ . The detailed experimental method is described in Appendix E. When  $t < 0$ , we set  $R_c = 5$  and particles are unfocused in all four channels. As  $R_c$  increases to 25, the particles become focused after a certain time that decreases with increasing  $\epsilon_w$ . Since  $R_c = U'_m l / \nu$ , where  $U'_m$  is twice the average velocity in the channel  $U'_a$ , we can estimate the equivalent length required for the focusing transition  $L_{focus}$  as  $L_{focus} = U'_a t$ .  $L_{focus}$  decreases with increasing channel amplitude.

## 7. Discussion

We begin this section by thanking J. Marshall (personal communication, April 2023) for the following scaling analysis. As a hallmark of the inertial lift effect, particles focus on two symmetric lines in our theory and experiments. By contrast, Hewitt & Marshall (2010) observed that particles focus on the centreline of a corrugated tube in their lubrication theory and discrete-element simulations. This discrepancy is resolved by the following

Case	$a/h$	$\epsilon_w \omega$	$R_c$	$\mathcal{R}$
A	0.06	0.628	40	6.580
B	0.01	0.628	400	39.478
C	0.01	0.314	400	9.870

Table 1. Values of ratio  $\mathcal{R}$  for DEM simulations in Hewitt & Marshall (2010).

scaling analysis, which provides a strategy to estimate the relative importance of the oscillatory straining and the inertial lift effects.

Our theory shows that the inertial lift force gives rise to a normalized lateral drift velocity  $U_{D,lift}$  relative to the particle-free flow, where  $U_{D,lift} = U'_{D,lift}/U'_m$ . Under the conditions  $a/h \ll 1$ ,  $\epsilon_w \ll 1$ , and  $\epsilon \ll 1$ , the drift velocity  $U_{D,lift} \sim O(R_c a^3/h^3)$ . Given the expression of the Stokes number  $Stk$  (5.3), we obtain

$$U_{D,lift} = O\left(Stk \frac{a}{h}\right). \tag{7.1}$$

Figure 6 indicates that the zeroth-order drift velocity in  $\epsilon_w$ ,  $U_{D,lift}^{(0)}$ , is directed away from the centreline for  $\mathcal{Z}_p < 0.6$ .

In the limit of a small channel Reynolds number ( $R_c \ll 1$ ) and a small slope of the waviness ( $\epsilon_w \omega \ll 1$ ), Hewitt & Marshall (2010) derived a normalized lateral drift velocity  $U_{D,osc}$  based on the oscillatory straining effect only

$$U_{D,osc} = O(Stk \epsilon_w^2 \omega^2). \tag{7.2}$$

The drift velocity  $U_{D,osc}$  is always directed toward the centreline regardless of the values of  $\mathcal{Z}_p$ . Thus,  $U_{D,lift}$  and  $U_{D,osc}$  compete against each other when a particle gets close to the centre part of the channel (e.g.  $\mathcal{Z}_p < 0.6$ ), and the particle's focusing location is determined by the relative importance of these two effects. Because  $U_{D,osc}/U_{D,lift} = O(\epsilon_w^2 \omega^2/(a/h))$ , we introduce

$$\mathcal{R} = \frac{\epsilon_w^2 \omega^2}{a/h}. \tag{7.3}$$

Although (7.1) and (7.2) are derived under a series of limiting conditions, the ratio  $\mathcal{R}$  can qualitatively characterize the relative importance of  $U_{D,lift}$  and  $U_{D,osc}$  when those conditions are not strictly satisfied.

The discrepancy between our study and Hewitt & Marshall (2010) can be explained by the different regimes of  $\mathcal{R}$  the two studies explore. Tables 1 and 2 show the values of  $\mathcal{R}$  for the three cases based on the discrete-element method (DEM) reported in Hewitt & Marshall (2010) and our experimental results in figure 11, respectively. The  $\mathcal{R}$ -values are significantly higher than unity in table 1, indicating that the oscillatory drift dominates over the inertial lift drift. Thus, particles focus on the centreline in Hewitt & Marshall (2010). In table 2, however, the  $\mathcal{R}$ -values are lower than or close to unity for the cases with  $\epsilon_w = 0.093$  and  $\epsilon_w = 0.249$ . Consequently, the inertial lift drift plays an important role, leading to separated focusing locations in figure 11. For  $\epsilon_w = 0.490$ , the  $\mathcal{R}$ -value is again significantly higher than unity. Due to the strong vortices in the channel, the conditions for both our asymptotic theory and the lubrication theory in Hewitt & Marshall (2010) break down; therefore, the scaling estimates in (7.1)–(7.3) are not reliable.

$\epsilon_w$	$a/h$	$\epsilon_w\omega$	$R_c$	$\mathcal{R}$
0.093	0.17	0.186	5–250	0.204
0.249	0.17	0.498	5–250	1.459
0.490	0.17	0.980	5–250	5.649

Table 2. Values of ratio  $\mathcal{R}$  for figure 11.

This scaling analysis also provides insight into the factors influencing the average focusing locations of the particles  $\bar{Z}_p$ . If  $a/h$  is held constant, an increase in  $\epsilon_w\omega$  results in an enhanced oscillatory effect; thus, the separation between the two focusing lines decreases (figures 11 and 12*b*). If  $\epsilon_w\omega$  is held constant, the influence of  $a/h$  on  $\bar{Z}_p$  is more complicated. As  $a/h$  decreases, an increased  $\mathcal{R}$  gives rise to a stronger oscillatory effect for inward drifting. However, a smaller  $a/h$  also leads to outward shifting in the absence of waviness (Di Carlo *et al.* 2009). In our explored parameter regime, figure 12*b* shows a prominent trend of outward shifting for a decreasing  $a/h$ . In future studies, a more accurate scaling analysis may shed light on the sophisticated influence of the relative particle size  $a/h$  on  $\bar{Z}_p$ .

## 8. Conclusions

We establish an asymptotic theory for particle focusing in wavy channels under the assumptions that the asymptotic parameter  $\epsilon = R_c^{1/2} a/l \ll 1$ , the normalized waviness amplitude  $\epsilon_w = (\epsilon_w h)/h \ll 1$  and the ratio between the particle radius and the half channel width  $a/h \ll 1$  (where  $R_c = U'_m l/\nu$  is the channel Reynolds number, and  $l = 2h$  is the channel width; see figure 3), and we experimentally investigate particle focusing at small-to-moderate  $\epsilon$ ,  $\epsilon_w$  and  $a/h$ . Our experimental measurements are not only consistent with our asymptotic theory but also demonstrate how the real focusing behaviour gradually deviates from the asymptotic results as we move away from the asymptotic limit.

In comparison with previous asymptotic theories on particle focusing in straight channels, we introduce a second asymptotic parameter  $\epsilon_w$  and approximate the lift force as  $F_{L,z}^{(0)} + \epsilon_w F_{L,z}^{(1)}$ . The zeroth-order lift force  $F_{L,z}^{(0)}$  is exactly the lift force obtained in a parabolic flow field, and the first-order lift force  $F_{L,z}^{(1)}$  stems from the interactions of the particle with both the zeroth-order Poiseuille flow and the first-order flow due to the waviness of the channel. We demonstrate that  $F_{L,z}^{(1)}$  does not play a significant role in determining either the focusing locations or the length of channels required for focusing  $L_{focus}$ . By inserting  $F_{L,z}^{(0)}$  and the particle-free flow into the simplified Maxey–Reily equation, we simulate particle trajectories and estimate the focusing locations of the particles. We derive this method based on asymptotic assumptions; surprisingly, it also provides reasonable estimates for more realistic situations with moderate  $\epsilon$ ,  $\epsilon_w$  and  $a/h$ . Consequently, one can predict the focusing locations with the zeroth-order lift force  $F_{L,z}^{(0)}$  and the particle-free flow in a wavy channel. This finding can be regarded as a synergy between the inertial lift and the oscillatory straining effects because the particle-free flow gives rise to the oscillatory straining effect. The relative importance of these two effects is influenced by parameters including the waviness frequency  $\omega$ , the amplitude  $\epsilon_w$  and the normalized particle size  $a/h$ . Under a stronger inertial lift effect, particles focus on two

widely separated symmetric lines; however, these two lines move closer to the centreline of the channel under a stronger oscillatory straining effect.

As in straight channels, the focusing locations of particles in wavy channels are functions of  $R_c$  and  $a/h$ . The corresponding conclusions from straight channels, however, may not be transferable to wavy channels. First, in straight channels, particles stabilize at the locations where the lift force vanishes. By contrast, since the lift force varies in the axial direction in wavy channels, the focusing locations are different from zero-lift-force locations (figures 8 and 11). Second, when  $R_c$  increases or  $a/h$  decreases, the focusing locations in straight channels simply shift outwards. This conclusion still holds true when wavy channels have a relatively low  $\epsilon_w$ . However, when  $\epsilon_w$  is above the order of 0.1, e.g.  $\epsilon_w = 0.490$  in figure 11, particles can move inwards as  $R_c$  increases. This phenomenon is attributed to the variations in the shape of the streamlines in the particle-free flow. When  $R_c$  is of order 100 or larger, vortices appear in the expanded sections of the wavy channels, and particles occasionally get trapped in these vortices. As in straight channels, the focusing locations of particles also shift outwards as  $a/h$  decreases. Additionally, the average focusing location in the  $z$ -direction  $\bar{Z}_p$  is negatively related to  $\epsilon_w$  and not significantly influenced by  $\omega$ .

Interestingly, our experiments reveal that particles focus slightly faster in wavy channels than in straight channels. Namely, at the same  $R_c$  and average channel width  $l$ , it requires a shorter channel length  $L$  for particles to be focused in wavy channels. Since this behaviour cannot be explained by the asymptotic theory, we attribute it to the finite particle size and the resultant unbalanced lift force in the expanded and contracted sections. This may shed light on new strategies to accelerate particle focusing in channels.

Last but not least, the variety of the focusing behaviour stems from the secondary flow introduced by the waviness. Our work lays the foundation for studying the influence of secondary flows in more general periodic channels.

**Supplementary movie.** A supplementary movie is available at <https://doi.org/10.1017/jfm.2023.558>.

**Acknowledgements.** We thank J. Marshall for his valuable scaling analysis and W. van Rees for helpful discussions. X.M. acknowledges B. Keshavarz, J.H. Cho, Q. Zhang, S. Yamani and P. Lilin for offering help with experimental facilities.

**Funding.** X.M. acknowledges the financial support from the National Institutes of Health (grant numbers 3U54EB015408-07S2, 3U54EB015408-08S2).

**Declaration of interests.** The authors report no conflict of interest.

**Author ORCIDiDs.**

 Xinyu Mao <https://orcid.org/0000-0003-1939-046X>;

 Irmgard Bischofberger <https://orcid.org/0000-0002-7067-6626>.

## Appendix A. Particle-free flow at infinitesimal channel Reynolds number

In this appendix, we calculate the first-order velocity components  $\bar{v}_x^{(1)}$  and  $\bar{v}_z^{(1)}$  at  $\mathcal{R} = 0$  in the Stokes-flow limit, i.e.  $R_c \rightarrow 0$ . Because fluid inertia vanishes in this limit, the left-hand sides of the momentum equations (2.5b) and (2.5c) become zero. To eliminate the pressure terms, we differentiate (2.5b) with respect to  $\mathcal{Z}$ , multiply (2.5c) with  $-i\omega$  and then add these two equations together, obtaining

$$0 = -\omega^2 \frac{d\hat{v}_x}{d\mathcal{Z}} + \frac{d^3\hat{v}_x}{d\mathcal{Z}^3} - i \left( -\omega^3 \hat{v}_z + \omega \frac{d^2\hat{v}_z}{d\mathcal{Z}^2} \right). \quad (\text{A1})$$

By introducing  $\hat{\mathcal{V}}_z = i\mathcal{W}$ , we rewrite (2.5a), (A1) and (2.5d) as

$$\omega \hat{\mathcal{V}}_x + \frac{d\mathcal{W}}{d\mathcal{Z}} = 0, \tag{A2a}$$

$$-\omega^2 \frac{d\hat{\mathcal{V}}_x}{d\mathcal{Z}} + \frac{d^3\hat{\mathcal{V}}_x}{d\mathcal{Z}^3} + \left(-\omega^3\mathcal{W} + \omega \frac{d^2\mathcal{W}}{d\mathcal{Z}^2}\right) = 0, \tag{A2b}$$

$$\hat{\mathcal{V}}_x = -2 \quad \text{and} \quad \mathcal{W} = 0 \quad \text{at} \quad \mathcal{Z} = \pm 1. \tag{A2c}$$

Solving (A2) with Mathematica, we have

$$\hat{\mathcal{V}}_x = \frac{4 \cosh(\omega\mathcal{Z}) [-\omega \cosh(\omega) + \sinh(\omega)] + 4\omega\mathcal{Z} \sinh(\omega) \sinh(\omega\mathcal{Z})}{2\omega - \sinh(2\omega)}. \tag{A3}$$

Equation (2.6) can then be obtained by inserting (A3) into the ansatz  $\bar{\mathcal{V}}_x^{(1)} = \text{Re}[\hat{\mathcal{V}}_x(\mathcal{Z}) \exp(i\omega\mathcal{X})]$ . Since  $\hat{\mathcal{V}}_x$  is a real-valued function of  $\mathcal{Z}$ , the component  $\hat{\mathcal{V}}_z$  is imaginary (2.5a) and  $\bar{\mathcal{V}}_z^{(1)}(\mathcal{X} = 0, \mathcal{Z}) = 0$ .

### Appendix B. Particle-free flow at infinitesimal waviness frequency

In this appendix, we analytically calculate the laminar particle-free velocity field at an infinitesimal angular frequency of the waviness, i.e.  $\omega' \rightarrow 0$  (the lubrication limit). Because the channel wavelength  $\lambda = 2\pi/\omega'$ , we assume  $h \ll \lambda$  and introduce the following dimensionless parameters:

$$\epsilon_h = \frac{h}{\lambda}, \quad \check{\mathcal{X}} = \frac{\mathcal{X}'}{\lambda}, \quad \check{\mathcal{Z}} = \frac{\mathcal{Z}'}{h}, \quad \check{\mathcal{V}}_x = \frac{\bar{\mathcal{V}}'_x}{U'_m}, \quad \check{\mathcal{V}}_z = \frac{\bar{\mathcal{V}}'_z}{\epsilon_h U'_m}, \quad \text{and} \quad \check{\mathcal{P}} = \frac{\bar{\mathcal{P}}' h^2}{\mu U'_m \lambda}, \tag{B1a-f}$$

where  $\epsilon_h \ll 1$ . The dimensionless Navier–Stokes equations and the continuity condition take the following forms:

$$\frac{1}{2} \epsilon_h R_c \left( \check{\mathcal{V}}_x \frac{\partial \check{\mathcal{V}}_x}{\partial \check{\mathcal{X}}} + \check{\mathcal{V}}_z \frac{\partial \check{\mathcal{V}}_x}{\partial \check{\mathcal{Z}}} \right) = -\frac{\partial \check{\mathcal{P}}}{\partial \check{\mathcal{X}}} + \epsilon_h^2 \frac{\partial^2 \check{\mathcal{V}}_x}{\partial \check{\mathcal{X}}^2} + \frac{\partial^2 \check{\mathcal{V}}_x}{\partial \check{\mathcal{Z}}^2}, \tag{B2a}$$

$$\frac{1}{2} \epsilon_h^3 R_c \left( \check{\mathcal{V}}_x \frac{\partial \check{\mathcal{V}}_z}{\partial \check{\mathcal{X}}} + \check{\mathcal{V}}_z \frac{\partial \check{\mathcal{V}}_z}{\partial \check{\mathcal{Z}}} \right) = -\frac{\partial \check{\mathcal{P}}}{\partial \check{\mathcal{Z}}} + \epsilon_h^4 \frac{\partial^2 \check{\mathcal{V}}_z}{\partial \check{\mathcal{X}}^2} + \epsilon_h^2 \frac{\partial^2 \check{\mathcal{V}}_z}{\partial \check{\mathcal{Z}}^2}, \tag{B2b}$$

$$\frac{\partial \check{\mathcal{V}}_x}{\partial \check{\mathcal{X}}} + \frac{\partial \check{\mathcal{V}}_z}{\partial \check{\mathcal{Z}}} = 0, \tag{B2c}$$

respectively. We enforce the same no-slip boundary condition as in (2.2)

$$\check{\mathcal{V}}_x = \check{\mathcal{V}}_z = 0 \quad \text{at} \quad \check{\mathcal{Z}} = \pm 1 \pm \delta(\check{\mathcal{X}}), \tag{B3}$$

where  $\delta(\check{\mathcal{X}}) = -\epsilon_w \cos(\check{\omega}\check{\mathcal{X}})$  and  $\check{\omega} = \omega'\lambda$ . Assuming  $\epsilon_h \ll \epsilon_w \ll 1$ , we expand  $\check{\mathcal{V}}_x$ ,  $\check{\mathcal{V}}_z$  and  $\check{\mathcal{P}}$  into Taylor series in  $\epsilon_h$

$$\check{\mathcal{V}}_x = \check{\mathcal{V}}_x^{(0)} + \epsilon_h \check{\mathcal{V}}_x^{(1)} + O(\epsilon_h^2), \tag{B4a}$$

$$\check{\mathcal{V}}_z = \check{\mathcal{V}}_z^{(0)} + \epsilon_h \check{\mathcal{V}}_z^{(1)} + O(\epsilon_h^2), \tag{B4b}$$

$$\check{\mathcal{P}} = \check{\mathcal{P}}^{(0)} + \epsilon_h \check{\mathcal{P}}^{(1)} + O(\epsilon_h^2), \tag{B4c}$$

and then solve (B2) and (B3) asymptotically. Note that the superscripts {0} and {1} denote orders in  $\epsilon_h$ . Here, we provide the derivation for the zeroth-order velocity in  $\epsilon_h$ . Based on (B2) we obtain the zeroth-order governing equations and boundary conditions

$$-\frac{\partial \check{\mathcal{P}}^{(0)}}{\partial \check{\mathcal{X}}} + \frac{\partial^2 \check{\mathcal{V}}_x^{(0)}}{\partial \check{\mathcal{Z}}^2} = 0, \tag{B5a}$$

$$\frac{\partial \check{\mathcal{P}}^{(0)}}{\partial \check{\mathcal{Z}}} = 0, \tag{B5b}$$

$$\frac{\partial \check{\mathcal{V}}_x^{(0)}}{\partial \check{\mathcal{X}}} + \frac{\partial \check{\mathcal{V}}_z^{(0)}}{\partial \check{\mathcal{Z}}} = 0, \tag{B5c}$$

$$\check{\mathcal{V}}_x^{(0)} = \check{\mathcal{V}}_z^{(0)} = 0, \quad \text{at } \check{\mathcal{Z}} = \pm 1 \pm \delta(\check{\mathcal{X}}). \tag{B5d}$$

We first integrate the momentum equation (B5a) with respect to  $\check{\mathcal{Z}}$ , obtaining

$$\check{\mathcal{V}}_x^{(0)} = \frac{1}{2} \frac{d\check{\mathcal{P}}^{(0)}}{d\check{\mathcal{X}}} [\check{\mathcal{Z}}^2 - (1 + \delta)^2]. \tag{B6}$$

Because of a constant flow rate  $Q$ , we integrate  $\check{\mathcal{V}}_x^{(0)}$  across the channel and obtain  $d\check{\mathcal{P}}^{(0)}/d\check{\mathcal{X}} = -3Q/[2(1 + \delta)^3]$ . After inserting  $\delta = -\epsilon_w \cos(\check{\omega}\check{\mathcal{X}})$  into (B6), we further expand  $\check{\mathcal{V}}_x^{(0)}$  into Taylor series in  $\epsilon_w$

$$\check{\mathcal{V}}_x^{(0)} = (1 - \check{\mathcal{Z}}^2) + \cos(\check{\omega}\check{\mathcal{X}})(1 - 3\check{\mathcal{Z}}^2)\epsilon_w + O(\epsilon_w)^2, \tag{B7}$$

where we have inserted  $Q = 4/3$  because the zeroth-order term in  $\epsilon_w$  has a magnitude of 1 for  $\check{\mathcal{Z}} = 0$ . We then integrate the continuity equation (B5c) with respect to  $\check{\mathcal{Z}}$  to obtain  $\check{\mathcal{V}}_z^{(0)}$ , which is also expanded into Taylor series in  $\epsilon_w$

$$\check{\mathcal{V}}_z^{(0)} = \check{\omega} \sin(\check{\omega}\check{\mathcal{X}})\check{\mathcal{Z}}(1 - \check{\mathcal{Z}}^2)\epsilon_w + O(\epsilon_w)^2. \tag{B8}$$

Any higher-order velocity in  $\epsilon_h$  is negligible compared with  $\check{\mathcal{V}}^{(0)}$ .

Finally, we derive (2.7a,b) based on (B7) and (B8). As  $\epsilon_h \rightarrow 0$ , the dimensionless velocity  $\check{\mathcal{V}}$  reduces to  $\check{\mathcal{V}}^{(0)}$ . Given  $\bar{\mathcal{V}} = \check{\mathcal{V}}/U'_m$  and (B1a-f), one can convert the symbols and find that

$$\bar{\mathcal{V}}_x \rightarrow (1 - \mathcal{Z}^2) + \cos(\omega\mathcal{X})(1 - 3\mathcal{Z}^2)\epsilon_w + O(\epsilon_w)^2 \quad \text{and} \quad \bar{\mathcal{V}}_z \rightarrow 0. \tag{B9a,b}$$

Inserting  $\mathcal{X} = 0$  into (B9a,b) and further collecting the first-order terms in  $\epsilon_w$  gives rise to (2.7a,b).

### Appendix C. Force balance on neutrally buoyant particle

Herein, we establish the balance of forces acting on the particle. We start with the laboratory frame, in which the acceleration of the particle is driven by the total force including the gravitational force and the integrated fluid stress over the particle surface

$$m_p \mathbf{a}' = -m_p g \mathbf{e}_y + \int_{|\boldsymbol{\mathcal{R}} - \boldsymbol{\mathcal{R}}_p| = a} \mathbf{n} \cdot (-\mathcal{P}' \mathbf{I} + \mu(\nabla' \boldsymbol{\mathcal{V}}' + (\nabla' \boldsymbol{\mathcal{V}}')^T)) dS', \tag{C1}$$

where  $\mathbf{n}$  is the unit outward normal on the particle surface,  $\mathcal{P}'$  is the disturbed fluid pressure in the laboratory frame and  $\boldsymbol{\mathcal{V}}'$  is the disturbed fluid velocity in the



laboratory frame. We assume the gravitational force is in the out-of-plane direction,  $-e_y$ . Again, the prime symbols denote quantities and operations in the dimensional space.

We now rewrite (C1) with symbols defined in the particle frame by inserting  $e_y = e_y$ ,  $\mathcal{P}' = p'$ ,  $\mathcal{V}' = U'_p + \mathbf{v}'$  and  $\mathbf{r}' = \mathcal{R}' - \mathcal{R}'_p$ . Additionally, the spatial gradient  $\nabla'$  can be used interchangeably for our two sets of dimensional coordinate systems. Introducing a virtual force  $-m_p \mathbf{a}'$  due to the acceleration of the frame, we have the following force balance:

$$-m_p g e_y + \int_{|r'|=a} \mathbf{n} \cdot (-p' \mathbf{I} + \mu(\nabla' \mathbf{v}' + (\nabla' \mathbf{v}')^T)) dS' - m_p \mathbf{a}' = \mathbf{0}. \quad (C2)$$

To separate the contributions from the undisturbed flow and the perturbation due to the particle, we further insert the perturbation velocity  $\mathbf{u}' = \mathbf{v}' - \bar{\mathbf{v}}'$  and the perturbation pressure  $q' = p' - \bar{p}'$  into (C2), obtaining

$$\begin{aligned} & -m_p g e_y + \int_{|r'|=a} \mathbf{n} \cdot (-\bar{p}' \mathbf{I} + \mu(\nabla' \bar{\mathbf{v}}' + (\nabla' \bar{\mathbf{v}}')^T)) dS' \\ & + \int_{|r'|=a} \mathbf{n} \cdot (-q' \mathbf{I} + \mu(\nabla' \mathbf{u}' + (\nabla' \mathbf{u}')^T)) dS' - m_p \mathbf{a}' = \mathbf{0}. \end{aligned} \quad (C3)$$

Under the assumption of a small particle, Maxey & Riley (1983) found that the first integral in (C3) gives rise to a buoyancy force  $m_f g e_y$  and the inertia of the fluid parcel that has been spatially replaced by the particle,  $m_f (D' \bar{\mathbf{V}}' / D' t')$ , where  $D' \bar{\mathbf{V}}' / D' t' = \mathbf{a}' + D' \bar{\mathbf{v}}' / D' t'$ . In the perturbation analysis by Maxey & Riley (1983), the momentum equation for  $\mathbf{u}'$  takes the form of an unsteady Stokes equation; thus, their perturbation field (corresponding to the second integral in (C3)) yields a drag force, an added mass force and a Basset force, where the latter two forces stem from the unsteadiness of the perturbation field. By contrast, our momentum equation (3.4a) contains the Oseen corrections, which give rise to an inertial lift force. Additionally, we neglect the time derivative in (3.4a) with a scaling argument in § 4.2. Thus, the force balance in (C3) reduces to

$$m_f \left( \frac{\partial' \bar{\mathbf{v}}'}{\partial' t'} + \bar{\mathbf{v}}' \cdot \nabla' \bar{\mathbf{v}}' \right) \Big|_{r'=0} + \mathbf{F}'_D + \mathbf{F}'_L = \mathbf{0}, \quad (C4)$$

where the term within the parentheses represents the difference between the inertia of the fluid parcel and that of the particle, and  $\mathbf{F}'_D$  and  $\mathbf{F}'_L$  denote the drag and lift forces, respectively. With  $\mathbf{u}' = \mathbf{v}' - \bar{\mathbf{v}}'$ ,  $\bar{\mathbf{v}}' = \bar{\mathbf{V}}' - U'_p$  and  $\mathbf{v}(\mathbf{r}' = \mathbf{0}) = \mathbf{0}$ , one can show that  $\mathbf{u}'(\mathbf{r}' = \mathbf{0}) = -\bar{\mathbf{v}}'(\mathbf{r}' = \mathbf{0}) = -\mathbf{V}'_s$ . Namely, in the particle frame, the perturbation velocity is identical to the negative of the undisturbed velocity at the particle centre as well as the negative of the slip velocity. Additionally, the drag force  $\mathbf{F}'_D = 6\pi a \mu (\bar{\mathbf{V}}'(\mathcal{R}'_p(t')) - U'_p) = 6\pi \mu a \bar{\mathbf{v}}'(\mathbf{r}' = \mathbf{0})$ . Since the characteristic time  $t'$  for the variation of the perturbation flow is  $l^2/\nu$ , we non-dimensionalize (C4) with

$$\bar{\mathbf{V}} = \frac{\bar{\mathbf{V}}'}{U'_m}, \quad \bar{\mathbf{v}} = \frac{\bar{\mathbf{v}}'}{U'_m}, \quad \nabla' = \frac{1}{h} \nabla, \quad \mathbf{F} = \frac{\mathbf{F}'}{\mu a U'_m}, \quad \text{and} \quad t = \frac{t'}{l^2/\nu}, \quad (C5a-e)$$

obtaining

$$\frac{8}{3} \pi \epsilon^2 \left( -\frac{1}{2} R_c^{-1} \frac{\partial \mathbf{u}}{\partial t} - \mathbf{u} \cdot \nabla \bar{\mathbf{V}} \right) \Big|_{r=0, \mathcal{R}=\mathcal{R}_p} - 6\pi \mathbf{u}(\mathbf{r} = \mathbf{0}) + \mathbf{F}_L = \mathbf{0}. \quad (C6)$$

Note that we convert the spatial gradient with the identity  $\nabla' \bar{\mathbf{v}}' = \nabla \bar{\mathbf{V}}'$  in deriving (C6). Because the perturbation velocity  $\mathbf{u}(\mathbf{r} = \mathbf{0}) = O(\epsilon^3)$ , the first term has a magnitude of

$O(\epsilon^5)$  and is negligible compared with  $-6\pi\mathbf{u}(\mathbf{r} = \mathbf{0})$  for  $\epsilon \ll 1$ . Consequently, the lift force  $F_L$  is given by

$$F_L = 6\pi\mathbf{u}(\mathbf{r} = \mathbf{0}) + O(\epsilon^5), \tag{C7}$$

which is consistent with previous work on particle focusing in a straight channel (Asmolov 1999; Matas *et al.* 2009). In principle, a lift force is perpendicular to the oncoming flow; therefore, we only consider the  $z$ -component  $F_{L,z}$  to determine the focusing locations in the  $z$ -direction. Furthermore, the perturbation velocity component  $u_z(\mathbf{r} = \mathbf{0})$  corresponds to the drift velocity relative to the undisturbed flow,  $U_{D,lift}$  in § 7.

#### Appendix D. Solving for $\tilde{U}_z^{(0)}$ and $\tilde{U}_z^{(1)}$ in Fourier domain

In this appendix, we discuss the details for deriving and solving the governing equations for  $\tilde{U}_z^{(0)}(k_x, k_y, Z)$  and  $\tilde{U}_z^{(1)}(k_x, k_y, Z)$ . We first derive the ODEs for  $\tilde{U}_z^{(0)}$  and  $\tilde{U}_z^{(1)}$  for arbitrary values of frequencies  $k_x$  and  $k_y$  in § D.1. We then provide the asymptotic results for  $\tilde{U}_z^{(0)}$  and  $\tilde{U}_z^{(1)}$  at large frequencies in § D.2.

##### D.1. Derivations of ODEs for $\tilde{U}_z^{(0)}$ and $\tilde{U}_z^{(1)}$

To evaluate (4.20), we take a Fourier transform in  $X$  and  $Y$  in which any function  $\xi(X, Y, Z)$  and its counterpart in the frequency domain  $\tilde{\xi}(k_x, k_y, Z)$  are related via

$$\tilde{\xi}(k_x, k_y, Z) = \frac{1}{4\pi^2} \int_{-\infty}^{\infty} \int_{-\infty}^{\infty} \xi(X, Y, Z) \exp(-i(k_x X + k_y Y)) dX dY, \tag{D1a}$$

$$\xi(X, Y, Z) = \int_{-\infty}^{\infty} \int_{-\infty}^{\infty} \tilde{\xi}(k_x, k_y, Z) \exp(i(k_x X + k_y Y)) dk_x dk_y. \tag{D1b}$$

By transforming (4.17), we arrive at the transformed governing equations for  $\tilde{U}^{(0)}(k_x, k_y, Z)$  and  $\tilde{Q}^{(0)}(k_x, k_y, Z)$

$$\begin{aligned} L\tilde{U}^{(0)} - \begin{pmatrix} ik_x \\ ik_y \\ d \\ dZ \end{pmatrix} \tilde{Q}^{(0)} - ik_x \bar{V}_x^{(0)} \tilde{U}^{(0)} - \frac{d\bar{V}_x^{(0)}}{dZ} \tilde{U}_z^{(0)} \mathbf{e}_x \\ = -\frac{5}{6\pi} R_c^{-1/2} \gamma \left[ \frac{d\delta(Z)}{dZ} \mathbf{e}_x + ik_x \delta(Z) \mathbf{e}_z \right], \end{aligned} \tag{D2a}$$

$$ik_x \tilde{U}_x^{(0)} + ik_y \tilde{U}_y^{(0)} + \frac{d\tilde{U}_z^{(0)}}{dZ} = 0, \tag{D2b}$$

$$\tilde{U}^{(0)} = \mathbf{0}, \quad \text{at } Z = Z_{\pm}, \tag{D2c}$$

where we have defined the operator  $L = d^2/dZ^2 - k_x^2 - k_y^2$ . Equation (D2) can be further transformed into an ODE for  $\tilde{U}_z^{(0)}$ . We first express  $\tilde{Q}^{(0)}$  as a function of  $\tilde{U}_z^{(0)}$  with the

$x$ - and  $y$ -components of (D2a), and then insert the expression of  $\tilde{Q}^{(0)}$  into the  $z$ -component of (D2a), obtaining

$$L^2 \tilde{U}_z^{(0)} - ik_x \bar{V}_x^{(0)} L \tilde{U}_z^{(0)} + ik_x \frac{d^2 \bar{V}_x^{(0)}}{dZ^2} \tilde{U}_z^{(0)} = ik_x \gamma R_c^{-1/2} \frac{5}{6\pi} \left[ \frac{d^2 \delta(Z)}{dZ^2} + k^2 \delta(Z) \right], \quad (D3a)$$

$$\tilde{U}_z^{(0)} = \frac{d\tilde{U}_z^{(0)}}{dZ} = 0, \quad \text{at } Z = Z_{\pm}. \quad (D3b)$$

The Dirac delta function and its derivative in (D3a) give rise to jump conditions at  $Z = 0$  denoted by  $[\cdot]_{0-}^{0+}$

$$\left[ \frac{d\tilde{U}_z^{(0)}}{dZ} \right]_{0-}^{0+} = i \frac{5}{6\pi} k_x \gamma R_c^{-1/2} \quad \text{and} \quad \left[ \frac{d^3 \tilde{U}_z^{(0)}}{dZ^3} \right]_{0-}^{0+} = i \frac{5}{2\pi} k_x k^2 \gamma R_c^{-1/2}. \quad (D4a,b)$$

Equations (D2)–(D4a,b) take similar forms as those in Asmolov (1999), which solve the focusing locations of an asymptotically small particle in a Poiseuille flow. Indeed, any higher-order solution vanishes when  $\epsilon_w \rightarrow 0$ , and our problem reduces to particle focusing in a straight channel.

As prerequisites for the first-order analysis in  $\epsilon_w$ , the ODEs, boundary conditions and jump conditions of  $\tilde{U}_x^{(0)}$  and  $\tilde{U}_y^{(0)}$  are as follows:

$$\begin{aligned} (L - ik_x \bar{V}_x^{(0)}) \tilde{U}_x^{(0)} &= \left( \frac{ik_x L + k_x^2 \bar{V}_x^{(0)}}{k^2} \frac{d}{dZ} + \frac{k_y^2}{k^2} \frac{d\bar{V}_x^{(0)}}{dZ} \right) \tilde{U}_z^{(0)} \\ &\quad - \frac{5}{6\pi} \frac{k_y^2}{k^2} \gamma R_c^{-1/2} \frac{d\delta(Z)}{dZ}, \end{aligned} \quad (D5a)$$

$$\begin{aligned} (L - ik_x \bar{V}_x^{(0)}) \tilde{U}_y^{(0)} &= \left( \frac{ik_y L + k_x k_y \bar{V}_x^{(0)}}{k^2} \frac{d}{dZ} - \frac{k_x k_y}{k^2} \frac{d\bar{V}_x^{(0)}}{dZ} \right) \tilde{U}_z^{(0)} \\ &\quad + \frac{5}{6\pi} \frac{k_x k_y}{k^2} \gamma R_c^{-1/2} \frac{d\delta(Z)}{dZ}, \end{aligned} \quad (D5b)$$

$$\tilde{U}_x^{(0)} = \tilde{U}_y^{(0)} = 0, \quad \text{at } Z = Z_{\pm}, \quad (D5c)$$

$$\left[ \tilde{U}_x^{(0)} \right]_{0-}^{0+} = -\frac{5}{6\pi} \gamma R_c^{-1/2}. \quad (D5d)$$

where  $k = (k_x^2 + k_y^2)^{1/2}$ . We now derive the ODE for  $\tilde{U}_z^{(1)}$ . Since  $\bar{V}_x^{(1)}$  and  $\bar{V}_z^{(1)}$  in (4.18a) contain sinusoidal components, we propose the ansatz

$$U^{(1)} = \frac{1}{2} U^{(1a)} \exp[i(\varphi_p + \kappa X)] + \frac{1}{2} U^{(1b)} \exp[-i(\varphi_p + \kappa X)], \quad (D6a)$$

$$Q^{(1)} = \frac{1}{2} Q^{(1a)} \exp[i(\varphi_p + \kappa X)] + \frac{1}{2} Q^{(1b)} \exp[-i(\varphi_p + \kappa X)] \quad (D6b)$$

to separate variables  $\mathcal{X}_p$  and  $\mathcal{Z}_p$ , i.e.  $U^{(1a)}(X, Y, Z)$ ,  $U^{(1b)}(X, Y, Z)$ ,  $Q^{(1a)}(X, Y, Z)$  and  $Q^{(1b)}(X, Y, Z)$  are influenced by  $\mathcal{Z}_p$  only. The transformed version of (D6a) is

$$\tilde{U}^{(1)}(k_x, k_y, Z) = \frac{1}{2} \exp(i\varphi_p) \tilde{U}^{(1a)}(\check{k}_x, k_y, Z) + \frac{1}{2} \exp(-i\varphi_p) \tilde{U}^{(1b)}(\hat{k}_x, k_y, Z), \quad (D7)$$

where  $\check{k}_x = k_x - \kappa$  and  $\hat{k}_x = k_x + \kappa$ .  $\tilde{U}^{(1a)}(\check{k}_x, k_y, Z)$  and  $\tilde{U}^{(1b)}(\hat{k}_x, k_y, Z)$  are governed by two sets of ‘mirrored’ differential equations

$$\begin{aligned}
 L\tilde{U}^{(1a)}(\check{k}_x) - \left( \frac{ik_x}{d} \right) \tilde{Q}^{(1a)}(\check{k}_x) - ik_x \bar{V}_x^{(0)} \tilde{U}^{(1a)}(\check{k}_x) - \frac{d\bar{V}_x^{(0)}}{dZ} \tilde{U}_z^{(1a)}(\check{k}_x) \mathbf{e}_x \\
 = R_c^{1/2} \left\{ \left( i\check{k}_x \hat{V}_x + \hat{V}_z \frac{d}{dZ} \right) \tilde{U}^{(0)}(\check{k}_x) - \left( ik_x \hat{V}_{x0} + \hat{V}_{z0} \frac{d}{dZ} \right) \tilde{U}^{(0)}(k_x) \right. \\
 \left. + \left[ i\kappa \tilde{U}_x^{(0)}(\check{k}_x) + \tilde{U}_z^{(0)}(\check{k}_x) \frac{d}{dZ} \right] \left( \hat{V}_x \mathbf{e}_x + \hat{V}_z \mathbf{e}_z \right) \right\} \\
 + \frac{5}{6\pi} R_c^{-1/2} \left[ ik_x \delta(Z) (-\zeta \mathbf{e}_z + 2\alpha_z \mathbf{e}_x) - \frac{d\delta(Z)}{dZ} (\zeta \mathbf{e}_x + 2\alpha_z \mathbf{e}_z) \right], \tag{D8a}
 \end{aligned}$$

$$\begin{aligned}
 L\tilde{U}^{(1b)}(\hat{k}_x) - \left( \frac{ik_x}{d} \right) \tilde{Q}^{(1b)}(\hat{k}_x) - ik_x \bar{V}_x^{(0)} \tilde{U}^{(1b)}(\hat{k}_x) - \frac{d\bar{V}_x^{(0)}}{dZ} \tilde{U}_z^{(1b)}(\hat{k}_x) \mathbf{e}_x \\
 = R_c^{1/2} \left\{ \left( i\hat{k}_x \bar{\hat{V}}_x + \bar{\hat{V}}_z \frac{d}{dZ} \right) \tilde{U}^{(0)}(\hat{k}_x) - \left( ik_x \bar{\hat{V}}_{x0} + \bar{\hat{V}}_{z0} \frac{d}{dZ} \right) \tilde{U}^{(0)}(k_x) \right. \\
 \left. + \left[ -i\kappa \tilde{U}_x^{(0)}(\hat{k}_x) + \tilde{U}_z^{(0)}(\hat{k}_x) \frac{d}{dZ} \right] \left( \bar{\hat{V}}_x \mathbf{e}_x + \bar{\hat{V}}_z \mathbf{e}_z \right) \right\} \\
 + \frac{5}{6\pi} R_c^{-1/2} \left[ ik_x \delta(Z) (-\bar{\zeta} \mathbf{e}_z + 2\bar{\alpha}_z \mathbf{e}_x) - \frac{d\delta(Z)}{dZ} (\bar{\zeta} \mathbf{e}_x + 2\bar{\alpha}_z \mathbf{e}_z) \right], \tag{D8b}
 \end{aligned}$$

where  $\hat{V}_{x/z} = \hat{V}_{x/z}(2ZR_c^{-1/2} + Z_p)$  and  $\hat{V}_{x/z0} = \hat{V}_{x/z}(Z_p)$ . Here,  $\bar{\hat{V}}_x, \bar{\hat{V}}_z, \bar{\hat{V}}_{x0}, \bar{\hat{V}}_{z0}, \bar{\zeta}$  and  $\bar{\alpha}_z$  denote the complex conjugates of  $\hat{V}_x, \hat{V}_z, \hat{V}_{x0}, \hat{V}_{z0}, \zeta$  and  $\alpha_z$ , respectively. Based on (4.18b) and (D6), we obtain the continuity conditions in the frequency domain

$$ik_x \tilde{U}_x^{(1a)}(\check{k}_x) + ik_y \tilde{U}_y^{(1a)}(\check{k}_x) + \frac{d}{dZ} \tilde{U}_z^{(1a)}(\check{k}_x) = 0, \tag{D9a}$$

$$ik_x \tilde{U}_x^{(1b)}(\hat{k}_x) + ik_y \tilde{U}_y^{(1b)}(\hat{k}_x) + \frac{d}{dZ} \tilde{U}_z^{(1b)}(\hat{k}_x) = 0. \tag{D9b}$$

By eliminating  $\tilde{U}_x^{(1a)}, \tilde{U}_x^{(1b)}, \tilde{U}_y^{(1a)}, \tilde{U}_y^{(1b)}, \tilde{Q}^{(1a)}$  and  $\tilde{Q}^{(1b)}$ , we obtain the following ODEs for  $\tilde{U}_z^{(1a)}$  and  $\tilde{U}_z^{(1b)}$ :

$$\begin{aligned}
 L^2 \tilde{U}_z^{(1a)}(\check{k}_x) - ik_x \bar{V}_x^{(0)} L \tilde{U}_z^{(1a)}(\check{k}_x) + ik_x \frac{d^2 \bar{V}_x^{(0)}}{dZ^2} \tilde{U}_z^{(1a)}(\check{k}_x) \\
 = R_c^{1/2} \left\{ \left[ \kappa k_x \left( \hat{V}'_x + \hat{V}_x \frac{d}{dZ} \right) - i\kappa \left( k^2 \hat{V}_z + \hat{V}'_z \frac{d}{dZ} + \hat{V}_z \frac{d^2}{dZ^2} \right) \right] \tilde{U}_x^{(0)}(\check{k}_x) \right\}
 \end{aligned}$$

*Particle focusing in a wavy channel*

$$\begin{aligned}
 & -\kappa k_y \left( \hat{v}'_x + \hat{v}_x \frac{d}{dZ} \right) \tilde{U}_y^{(0)}(\check{k}_x) - \left[ \left( ik_x \hat{v}_{x0} + \hat{v}_{z0} \frac{d}{dZ} \right) L \right] \tilde{U}_z^{(0)}(k_x) \\
 & + \left[ ik_k k^2 \hat{v}_x - ik_x \hat{v}''_x + \left( ik_x \hat{v}_x + \hat{v}_z \frac{d}{dZ} + \hat{v}'_z \right) L \right] \tilde{U}_z^{(0)}(\check{k}_x) \Big\}, \tag{D10a}
 \end{aligned}$$

$$\begin{aligned}
 & L^2 \tilde{U}_z^{(1b)}(\hat{k}_x) - ik_x \bar{v}_x^{(0)} L \tilde{U}_z^{(1b)}(\hat{k}_x) + ik_x \frac{d^2 \bar{v}_x^{(0)}}{dZ^2} \tilde{U}_z^{(1b)}(\hat{k}_x) \\
 & = R_c^{1/2} \left\{ \left[ -\kappa k_x \left( \bar{v}'_x + \bar{v}_x \frac{d}{dZ} \right) + ik \left( k^2 \bar{v}_z + \bar{v}'_z \frac{d}{dZ} + \bar{v}_z \frac{d^2}{dZ^2} \right) \right] \tilde{U}_x^{(0)}(\hat{k}_x) \right. \\
 & + \kappa k_y \left( \bar{v}'_x + \bar{v}_x \frac{d}{dZ} \right) \tilde{U}_y^{(0)}(\hat{k}_x) - \left[ \left( ik_x \bar{v}_{x0} + \bar{v}_{z0} \frac{d}{dZ} \right) L \right] \tilde{U}_z^{(0)}(k_x) \\
 & \left. + \left[ -ik k^2 \bar{v}_x - ik_x \bar{v}''_x + \left( ik_x \bar{v}_x + \bar{v}_z \frac{d}{dZ} + \bar{v}'_z \right) L \right] \tilde{U}_z^{(0)}(\hat{k}_x) \right\}. \tag{D10b}
 \end{aligned}$$

The corresponding jump conditions are

$$\left. \begin{aligned}
 \left[ \frac{d\tilde{U}_z^{(1a)}}{dZ} \right]_{0-}^{0+} &= i \frac{5}{6\pi} \zeta k_x R_c^{-1/2}, & \left[ \frac{d\tilde{U}_z^{(1b)}}{dZ} \right]_{0-}^{0+} &= i \frac{5}{6\pi} \bar{\zeta} k_x R_c^{-1/2}, \\
 \left[ \frac{d^2 \tilde{U}_z^{(1a)}}{dZ^2} \right]_{0-}^{0+} &= \frac{5}{3\pi} \alpha_z (k^2 + k_x^2) R_c^{-1/2}, & \left[ \frac{d^2 \tilde{U}_z^{(1b)}}{dZ^2} \right]_{0-}^{0+} &= \frac{5}{3\pi} \bar{\alpha}_z (k^2 + k_x^2) R_c^{-1/2}, \\
 \left[ \frac{d^3 \tilde{U}_z^{(1a)}}{dZ^3} \right]_{0-}^{0+} &= i \zeta \frac{5}{2\pi} k_x k^2 R_c^{-1/2}, & \left[ \frac{d^3 \tilde{U}_z^{(1b)}}{dZ^3} \right]_{0-}^{0+} &= i \bar{\zeta} \frac{5}{2\pi} k_x k^2 R_c^{-1/2},
 \end{aligned} \right\} \tag{D11a}$$

where  $k^2 = k_x^2 + k_y^2$ ,  $\hat{v}'_{x/z} = d\hat{v}_{x/z}(2ZR_c^{-1/2} + \mathcal{Z}_p)/dZ$  and  $\hat{v}''_x = d^2\hat{v}_x(2ZR_c^{-1/2} + \mathcal{Z}_p)/dZ^2$ . The boundary conditions of  $\tilde{U}_z^{(1a/b)}$  and their first-order derivatives are also given at the average locations of the walls

$$\left. \begin{aligned}
 \tilde{U}_z^{(1a)}(\check{k}_x, k_y, Z_{\pm}) &= \pm \frac{1}{2} R_c^{1/2} \tilde{U}_z^{(0)'}(\check{k}_x, k_y, Z) \Big|_{Z=Z_{\pm}}, \\
 \tilde{U}_z^{(1a)'}(\check{k}_x, k_y, Z_{\pm}) &= \pm \frac{1}{2} R_c^{1/2} \tilde{U}_z^{(0)''}(\check{k}_x, k_y, Z) \Big|_{Z=Z_{\pm}},
 \end{aligned} \right\} \tag{D12a}$$

$$\left. \begin{aligned}
 \tilde{U}_z^{(1b)}(\hat{k}_x, k_y, Z_{\pm}) &= \pm \frac{1}{2} R_c^{1/2} \tilde{U}_z^{(0)'}(\hat{k}_x, k_y, Z) \Big|_{Z=Z_{\pm}}, \\
 \tilde{U}_z^{(1b)'}(\hat{k}_x, k_y, Z_{\pm}) &= \pm \frac{1}{2} R_c^{1/2} \tilde{U}_z^{(0)''}(\hat{k}_x, k_y, Z) \Big|_{Z=Z_{\pm}}.
 \end{aligned} \right\} \tag{D12b}$$

*D.2. Asymptotic analysis at large frequency in Fourier domain*

To numerically evaluate the double integrals in (4.21), we introduce polar coordinates  $(k, \theta)$  to replace the variables  $k_x$  and  $k_y$ , where  $k_x = k \cos \theta$  and  $k_y = k \sin \theta$ . As  $k \rightarrow +\infty$ ,  $\tilde{U}_z^{(0)}$ ,  $\tilde{U}_z^{(1a)}$  and  $\tilde{U}_z^{(1b)}$  asymptote to the transformed strainlet velocity fields, and we can analytically obtain their values at the origin.

Herein, we provide an overview of the asymptotic analysis for  $\tilde{U}_x^{(0)}(k, \theta, Z = 0)$ ,  $\tilde{U}_y^{(0)}(k, \theta, Z = 0)$  and  $\tilde{U}_z^{(0/1)}(k, \theta, Z = 0)$  at a large  $k$ . We introduce an asymptotic parameter  $\varepsilon = 1/k$  and rescale the  $Z$ -coordinate with  $\eta = Z/\varepsilon$ . We define  $\tilde{U}(Z) = f(\eta)$  and still use subscripts  $x/y/z$  and superscripts  $(0/1)$  to denote velocity components and orders in  $\varepsilon_w$ , respectively. When  $k \rightarrow +\infty$ , we have  $\varepsilon \rightarrow 0$ . Thus, we expand  $f$  in powers of  $\varepsilon$ , e.g.

$$f_z^{(0)}(\eta) = f_{z0}^{(0)}(\eta) + \varepsilon f_{z1}^{(0)}(\eta) + \varepsilon^2 f_{z2}^{(0)}(\eta) + \varepsilon^3 f_{z3}^{(0)}(\eta) + O(\varepsilon^4), \tag{D13}$$

where the additional subscripts  $0, 1, 2 \dots$  denote the orders in  $\varepsilon$ . The ODEs (D3), (D5) and (D10) are then expanded in orders of  $\varepsilon$  and reformulated with variable  $\eta$ . Unless  $\eta_{wall} = o(\varepsilon)$ , i.e. the particle is extremely close to the walls, the boundary conditions of these ODEs vanish. When solving the ODEs, we use the jump conditions at  $\eta = 0$  to determine the parameters of the solution.

We now provide the asymptotic results that are necessary for the calculation of  $F_{L,z}$  in (4.21). First, for the zeroth-order solution in  $\varepsilon_w$ , the transformed velocity at the origin is of  $O(\varepsilon^3)$

$$f_z^{(0)}(\eta = 0) = -\varepsilon^3 \frac{15}{8\pi} \cos^2 \theta \gamma R_c^{-1}. \tag{D14}$$

Since  $f^{(0)}(\eta)$  is essential to the asymptotic analysis of the first-order problem in  $\varepsilon_w$ , the leading-order approximations of  $f^{(0)}(\eta)$  are given by

$$f_z^{(0)}(\eta \geq 0) \simeq -i\frac{1}{2}s \cos \theta \eta e^{-\eta}, \quad f_z^{(0)}(\eta < 0) \simeq i\frac{1}{2}s \cos \theta \eta e^{\eta}, \tag{D15a}$$

$$f_x^{(0)}(\eta \geq 0) \simeq \frac{1}{2}s(1 - \cos^2 \theta \eta)e^{-\eta}, \quad f_x^{(0)}(\eta < 0) \simeq -\frac{1}{2}s(1 + \cos^2 \theta \eta)e^{\eta}, \tag{D15b}$$

$$f_y^{(0)}(\eta \geq 0) \simeq -\frac{1}{2}s \cos \theta \sin \theta \eta e^{-\eta}, \quad f_y^{(0)}(\eta < 0) \simeq -\frac{1}{2}s \cos \theta \sin \theta \eta e^{\eta}, \tag{D15c}$$

where  $s = -5\gamma R_c^{-1/2}/(6\pi)$  is a constant. It is important to note that three different frequencies appear in (D10), i.e.  $k$ ,  $\check{k}$  and  $\hat{k}$ . Consequently, we replace  $(\eta, \theta)$  in (D15) with  $(\check{\eta}, \check{\theta})$  and  $(\hat{\eta}, \hat{\theta})$  when inserting  $f^{(0)}(\eta)$  into (D10a) and (D10b), respectively. Here,

$$\check{\eta} = \check{\delta}\eta, \quad \hat{\eta} = \hat{\delta}\eta, \tag{D16a}$$

$$\check{\theta} = \arccos[\check{\delta}^{-1}(\cos \theta - \varepsilon\kappa)], \quad \hat{\theta} = \arccos[\hat{\delta}^{-1}(\cos \theta + \varepsilon\kappa)], \tag{D16b}$$

where  $\check{\delta} = \sqrt{1 - 2\varepsilon\kappa \cos \theta + \varepsilon^2\kappa^2}$  and  $\hat{\delta} = \sqrt{1 + 2\varepsilon\kappa \cos \theta + \varepsilon^2\kappa^2}$ . We calculate the transformed velocity at the origin using Mathematica, yielding

$$f_{z2}^{(1a)}(\eta = 0) = \frac{5}{24\pi} \gamma \hat{\nu}_{x0\kappa} \cos \theta \cos 2\theta, \tag{D17a}$$

$$f_{z2}^{(1b)}(\eta = 0) = -\frac{5}{24\pi} \gamma \overline{\hat{\nu}_{x0\kappa}} \cos \theta \cos 2\theta, \tag{D17b}$$

$$\tilde{U}_z^{(1a)}(Z) \simeq \varepsilon^2 f_{z2}^{(1a)}(\eta) \quad \text{and} \quad \tilde{U}_z^{(1b)}(Z) \simeq \varepsilon^2 f_{z2}^{(1b)}(\eta). \tag{D17c}$$

Although the second-order solutions  $f_{z2}^{(1a)}(\eta = 0)$  and  $f_{z2}^{(1b)}(\eta = 0)$  are non-zero, they cancel each other in (4.21). Thus, the first-order lift force in  $\varepsilon_w$  is determined by

$\varepsilon^3 f_{z3}^{(1a)}(\eta = 0)$  and  $\varepsilon^3 f_{z3}^{(1b)}(\eta = 0)$ , where

$$f_{z3}^{(1a)}(\eta = 0) = \frac{5}{512\pi} R_c^{-1} \left[ -96\zeta + 12\beta_x\gamma - R_c \hat{\mathcal{V}}_{x0}\gamma\kappa^2 + 4 \left( -24\zeta + 3\beta_x\gamma - 7R_c \hat{\mathcal{V}}_{x0}\gamma\kappa^2 \right) \cos 2\theta + 5R_c \hat{\mathcal{V}}_{x0}\gamma\kappa^2 \cos 4\theta \right], \quad (\text{D18a})$$

$$f_{z3}^{(1b)}(\eta = 0) = \frac{5}{512\pi} R_c^{-1} \left[ -96\bar{\zeta} + 12\bar{\beta}_x\gamma - R_c \overline{\hat{\mathcal{V}}}_{x0}\gamma\kappa^2 + 4 \left( -24\bar{\zeta} + 3\bar{\beta}_x\gamma - 7R_c \overline{\hat{\mathcal{V}}}_{x0}\gamma\kappa^2 \right) \cos 2\theta + 5R_c \overline{\hat{\mathcal{V}}}_{x0}\gamma\kappa^2 \cos 4\theta \right]. \quad (\text{D18b})$$

Here,  $\beta_x$  is a factor determined in (3.12).

### Appendix E. Experimental methods

This appendix introduces our methods for particle focusing experiments. We use two types of particles: polystyrene spherical particles (Maxi-Blast, PB-4) with an average diameter of 200  $\mu\text{m}$  and polyamide particles (LaVision) with an average diameter of 60  $\mu\text{m}$ . The standard deviations of the particle diameters are 12  $\mu\text{m}$  and 10  $\mu\text{m}$ , respectively. The particles are suspended in water–glycerol solutions, and the volume fraction of the particles is chosen to be 0.05 % to minimize interparticle interactions (for figure 11). We match the densities of the suspensions to the particle densities, i.e. 1.05  $\text{kg m}^{-3}$  for polystyrene particles and 1.03  $\text{kg m}^{-3}$  for polyamide particles by using water–glycerol mixtures with volume fractions of water of 81 % and 88 %, respectively, at a room temperature of 22 °C. 0.5 % v/v of Tween 20 (Sigma-Aldrich) is added to avoid clustering of particles.

We fabricate the straight and wavy channels by laser cutting acrylic sheets (Universal Laser Systems) and then seal the channels with 3M adhesive transfer tapes and epoxy glue. Both channels have an average width  $l = 1.18$  mm, depth  $w = 6.60$  mm and a length of 570 mm. The normalized amplitudes  $\varepsilon_w$  of the wavy channels are measured to be 0.093, 0.249 and 0.490. We hold the normalized frequency  $\omega$  of the wavy channels to be 2 ( $\omega = \omega'/h$ , see (3.6)). Figure 10(a) shows the experimental set-up. The channel is connected to one or two 60 ml syringes and a reservoir via tubes with an inner diameter of 3.18 mm. A syringe pump (Harvard PHD Ultra) drives the suspensions through the tubes at a flow rate of no more than 100  $\text{ml min}^{-1}$ . To observe particle focusing, we choose a location that is 550 mm downstream from the channel inlet. Depending on the flow rate, we image the flow using either a digital camera (LUMIX DC-GH5) or a high-speed camera (Phantom Miro M320S) mounted onto a microscope (Nikon Eclipse TE2000-U equipped with a Plan Fluor 4X/0.13 NA objective). We choose the digital camera for flow rates lower than 10  $\text{ml min}^{-1}$ ; for flow rates higher than 10  $\text{ml min}^{-1}$ , we set the frame rate of the high-speed camera to be 100–300 frames per second. Figure 10(b) shows four examples of a polystyrene particle in the channels captured by the high-speed camera. We analyse the images with ImageJ (NIH) to determine the locations of the particles and channel boundaries. For figure 11, we analyse images that contain only one particle.

Figure 13 shows the experimental method to determine the time required for focusing transition when the channel Reynolds number  $R_c$  is subject to a step function of time (figure 12c). We choose polystyrene particles and increase the particle volume fraction to be 0.2 % to guarantee a large enough number of particles for analysis. We set the focal

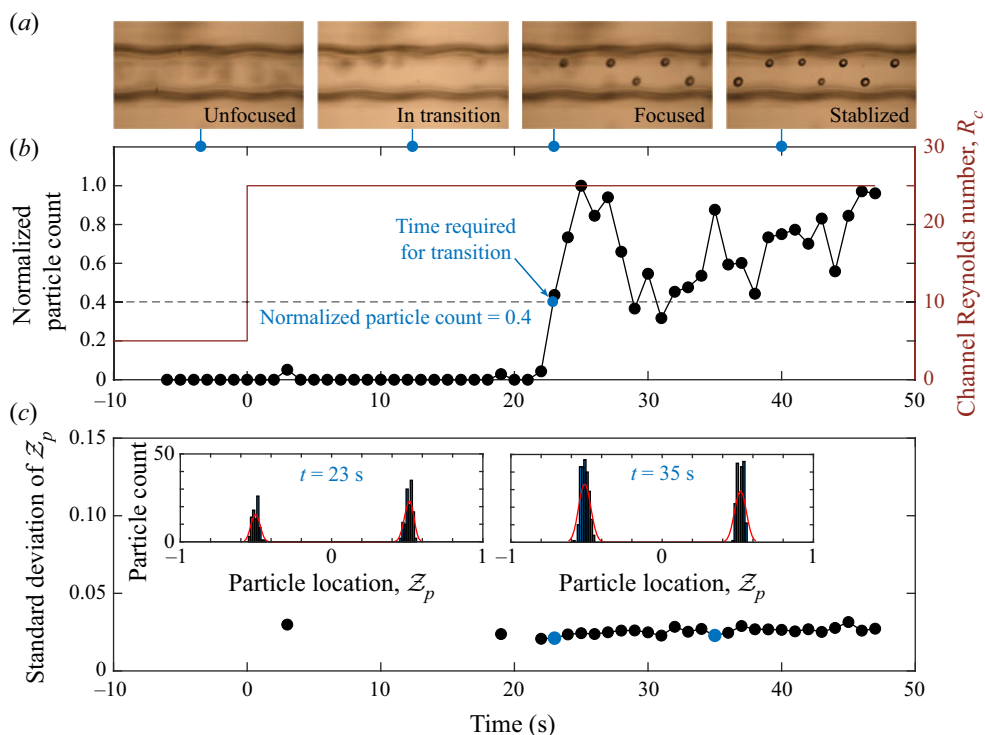


Figure 13. Determination of the time required for focusing transition after the channel Reynolds number increases from 5 to 25 at time  $t = 0$ . (a) Snapshots of the flow in different states in the wavy channel with  $\epsilon_w = 0.093$ . (b) Normalized number of particles captured by the camera over time. The time required for focusing transition is the first time at which the normalized particle count reaches 0.4. (c) Standard deviation of particle locations in the  $z$ -direction  $Z_p$  vs time. The online supplementary movie 1 shows particle focusing in a wavy channel occurring as the channel Reynolds number increases as a step function of time.

plane of the microscope at a height where particles will be focused at  $R_c = 25$ . When  $R_c = 5$ , there is little or no focusing. Additionally, due to the low flow rate and the slight difference in the densities between the particles and the solution, particles are out of focus by the time they reach the observation location. Thus, the camera can only capture vague images of particles, and ImageJ cannot identify the particle locations (figure 13a). After  $R_c$  increases from 5 to 25, particles are gradually focused. We count the number of particles identified within each second and normalize it with the maximal value (figure 13b). At a certain moment, the normalized particle count increases sharply from almost zero to the level of 0.5–1, and we determine the transition time with a normalized particle count of 0.4. The fluctuation of the particle count after focusing transition is largely due to a small interval of 1 s and the randomness of the particles. We further calculate the standard deviation of the  $z$ -locations of the particles  $Z_p$  over time (figure 13c). A stabilized standard deviation indicates that particles are indeed focused at the transition time.

#### REFERENCES

- AMINI, H., SOLLIER, E., MASAELI, M., XIE, Y., GANAPATHYSUBRAMANIAN, B., STONE, H.A. & DI CARLO, D. 2013 Engineering fluid flow using sequenced microstructures. *Nat. Commun.* **4** (1), 1826.  
 ASMOLOV, E.S. 1999 The inertial lift on a spherical particle in a plane Poiseuille flow at large channel Reynolds number. *J. Fluid Mech.* **381**, 63–87.



- ASMOLOV, E.S., DUBOV, A.L., NIZKAYA, T.V., HARTING, J. & VINOGRADOVA, O.I. 2018 Inertial focusing of finite-size particles in microchannels. *J. Fluid Mech.* **840**, 613–630.
- BAZAZ, S.R., MASHHADIAN, A., EHSANI, A., SAHA, S.C., KRÜGER, T. & WARKIANI, M.E. 2020 Computational inertial microfluidics: a review. *Lab on a Chip* **20**, 1023–1048.
- BHAGAT, A.A.S., KUNTAEGOWDANAHALLI, S.S. & PAPAUTSKY, I. 2008 Continuous particle separation in spiral microchannels using dean flows and differential migration. *Lab on a Chip* **8**, 1906–1914.
- CONTE, S.D. 1966 The numerical solution of linear boundary value problems. *SIAM Rev.* **8** (3), 309–321.
- COX, R.G. & BRENNER, H. 1968 The lateral migration of solid particles in Poiseuille flow – I theory. *Chem. Engng Sci.* **23** (2), 147–173.
- DI CARLO, D., EDD, J.F., HUMPHRY, K.J., STONE, H.A. & TONER, M. 2009 Particle segregation and dynamics in confined flows. *Phys. Rev. Lett.* **102**, 094503.
- DI CARLO, D., EDD, J.F., IRIMIA, D., TOMPKINS, R.G. & TONER, M. 2008 Equilibrium separation and filtration of particles using differential inertial focusing. *Anal. Chem.* **80** (6), 2204–2211.
- DI CARLO, D., IRIMIA, D., TOMPKINS, R.G. & TONER, M. 2007 Continuous inertial focusing, ordering, and separation of particles in microchannels. *Proc. Natl Acad. Sci. USA* **104** (48), 18892–18897.
- FERRY, J. & BALACHANDAR, S. 2001 A fast Eulerian method for disperse two-phase flow. *Intl J. Multiphase Flow* **27** (7), 1199–1226.
- GARCIA, M., GANAPATHYSUBRAMANIAN, B. & PENNATHUR, S. 2019 A linearised model for calculating inertial forces on a particle in the presence of a permeate flow. *J. Fluid Mech.* **861**, 253–274.
- GARCIA, M. & PENNATHUR, S. 2017 Inertial particle dynamics in the presence of a secondary flow. *Phys. Rev. Fluids* **2**, 042201.
- GUAZZELLI, É. & MORRIS, J.F. 2011 *A Physical Introduction to Suspension Dynamics*, 1st edn, pp. 28–51. Cambridge University Press.
- HA, K., HARDING, B., BERTOZZI, A.L. & STOKES, Y.M. 2022 Dynamics of small particle inertial migration in curved square ducts. *SIAM J. Appl. Dyn. Syst.* **21** (1), 714–734.
- HARDING, B. & STOKES, Y.M. 2020 Inertial focusing of non-neutrally buoyant spherical particles in curved microfluidic ducts. *J. Fluid Mech.* **902**, A4.
- HARDING, B., STOKES, Y.M. & BERTOZZI, A.L. 2019 Effect of inertial lift on a spherical particle suspended in flow through a curved duct. *J. Fluid Mech.* **875**, 1–43.
- HEWITT, G.F. & MARSHALL, J.S. 2010 Particle focusing in a suspension flow through a corrugated tube. *J. Fluid Mech.* **660**, 258–281.
- HO, B.P. & LEAL, L.G. 1974 Inertial migration of rigid spheres in two-dimensional unidirectional flows. *J. Fluid Mech.* **65** (2), 365–400.
- HOGG, A.J. 1994 The inertial migration of non-neutrally buoyant spherical particles in two-dimensional shear flows. *J. Fluid Mech.* **272**, 285–318.
- HOOD, K., LEE, S. & ROPER, M. 2015 Inertial migration of a rigid sphere in three-dimensional Poiseuille flow. *J. Fluid Mech.* **765**, 452–479.
- KIM, J., LEE, J., WU, C., NAM, S., DI CARLO, D. & LEE, W. 2016 Inertial focusing in non-rectangular cross-section microchannels and manipulation of accessible focusing positions. *Lab on a Chip* **16**, 992–1001.
- KUNDU, P., COHEN, I. & DOWLING, D. 2016 *Fluid Mechanics*, 6th edn, pp. 84–88 & 132–137. Academic.
- MARSHALL, J.S. 2009 Particle clustering in periodically forced straining flows. *J. Fluid Mech.* **624**, 69–100.
- MATAS, J., MORRIS, J.F. & GUAZZELLI, É. 2004 Inertial migration of rigid spherical particles in Poiseuille flow. *J. Fluid Mech.* **515**, 171–195.
- MATAS, J., MORRIS, J.F. & GUAZZELLI, É. 2009 Lateral force on a rigid sphere in large-inertia laminar pipe flow. *J. Fluid Mech.* **621**, 59–67.
- MAXEY, M.R. & RILEY, J.J. 1983 Equation of motion for a small rigid sphere in a nonuniform flow. *Phys. Fluids* **26** (4), 883–889.
- MORITA, Y., ITANO, T. & SUGIHARA-SEKI, M. 2017 Equilibrium radial positions of neutrally buoyant spherical particles over the circular cross-section in Poiseuille flow. *J. Fluid Mech.* **813**, 750–767.
- NAKAYAMA, S., YAMASHITA, H., YABU, T., ITANO, T. & SUGIHARA-SEKI, M. 2019 Three regimes of inertial focusing for spherical particles suspended in circular tube flows. *J. Fluid Mech.* **871**, 952–969.
- NIZKAYA, T., ANGIPELLA, J.R. & BUÈS, M.A. 2014 Inertial focusing of small particles in wavy channels: asymptotic analysis at weak particle inertia. *Physica D* **268**, 91–99.
- NIZKAYA, T.V., ASMOLOV, E.S., HARTING, J. & VINOGRADOVA, O.I. 2020 Inertial migration of neutrally buoyant particles in superhydrophobic channels. *Phys. Rev. Fluids* **5**, 014201.
- PARK, J., SONG, S. & JUNG, H. 2009 Continuous focusing of microparticles using inertial lift force and vorticity via multi-orifice microfluidic channels. *Lab on a Chip* **9**, 939–948.
- SAFFMAN, P.G. 1965 The lift on a small sphere in a slow shear flow. *J. Fluid Mech.* **22** (2), 385–400.

- SCHONBERG, J.A. & HINCH, E.J. 1989 Inertial migration of a sphere in Poiseuille flow. *J. Fluid Mech.* **203**, 517–524.
- SCOTT, M.R. & WATTS, H.A. 1977 Computational solution of linear two-point boundary value problems via orthonormalization. *SIAM J. Numer. Anal.* **14** (1), 40–70.
- SEGRÉ, G & SILBERBERG, A 1961 Radial particle displacements in Poiseuille flow of suspensions. *Nature* **189** (4760), 209–210.
- SELVARAJAN, S., TULAPURKARA, E.G. & VASANTA RAM, V. 1998 A numerical study of flow through wavy-walled channels. *Intl J. Numer. Meth. Fluids* **26** (5), 519–531.
- SELVARAJAN, S., TULAPURKARA, E.G. & VASANTA RAM, V. 1999 Stability characteristics of wavy walled channel flows. *Phys. Fluids* **11** (3), 579–589.
- STOECKLEIN, D. & DI CARLO, D. 2019 Nonlinear microfluidics. *Anal. Chem.* **91** (1), 296–314.
- SU, J., CHEN, X., ZHU, Y. & HU, G. 2021 Machine learning assisted fast prediction of inertial lift in microchannels. *Lab on a Chip* **21**, 2544–2556.
- TANG, W., ZHU, S., JIANG, D., ZHU, L., YANG, J. & XIANG, N. 2020 Channel innovations for inertial microfluidics. *Lab on a Chip* **20**, 3485–3502.
- VALANI, R.N., HARDING, B. & STOKES, Y.M. 2022 Bifurcations and dynamics in inertial focusing of particles in curved rectangular ducts. *SIAM J. Appl. Dyn. Syst.* **21** (4), 2371–2392.
- VAN DYKE, M. 1975 *Perturbation Methods in Fluid Mechanics*, 1st edn, p. 37. Parabolic.
- ZHANG, J., YAN, S., YUAN, D., ALICI, G., NGUYEN, N., EBRAHIMI WARKIANI, M. & LI, W. 2016 Fundamentals and applications of inertial microfluidics: a review. *Lab on a Chip* **16**, 10–34.
- ZHANG, T., *et al.* 2021 Hydrodynamic particle focusing enhanced by femtosecond laser deep grooving at low Reynolds numbers. *Sci. Rep.* **11** (1), 1652.
- ZHOU, J., KASPER, S. & PAPAUTSKY, I. 2013 Enhanced size-dependent trapping of particles using microvortices. *Microfluid Nanofluid* **15** (5), 611–623.